Super-Cluster collimation for ultra-sensitive SPECT-PET
a simulation study

Cosmi, Valerio; Ghosh, Satyajit; Ramakers, Ruud M.; Goorden, Marlies C.; Beekman, Freek J.

DOI
10.1088/1361-6560/ae2e7a

Publication date
2025

Document Version
Final published version

Published in
Physics in medicine and biology

Physics in Medicine & Biology

PAPER • OPEN ACCESS

Super-Cluster collimation for ultra-sensitive SPECT-PET: a simulation study

To cite this article: Valerio Cosmi *et al* 2026 *Phys. Med. Biol.* **71** 015015

IOP Publishing Phys. Med. Biol. 71 (2026) 015015 https://doi.org/10.1088/1361-6560/ae2e7a

Physics in Medicine & Biology

IPEM Institute of Physics and Engineering in Medicine

OPEN ACCESS

RECEIVED
6 August 2025

REVISED
9 December 2025

ACCEPTED FOR PUBLICATION
17 December 2025

PUBLISHED
30 December 2025

PAPER

Super-Cluster collimation for ultra-sensitive SPECT-PET: a simulation study

Valerio Cosmi[1], **Satyajit Ghosh**[1], **Ruud M Ramakers**[1,2], **Marlies C Goorden**[1,*] **and Freek J Beekman**[1,3,4]

[1] Department of Radiation Science and Technology, Delft University of Technology, Delft, The Netherlands
[2] MILabs B.V., Houten, The Netherlands
[3] Free Bee International, Gouda, The Netherlands
[4] The Molecular Imaging Foundation, Gouda, The Netherlands
[*] Author to whom any correspondence should be addressed.

E-mail: m.c.goorden@tudelft.nl

Keywords: SPECT, PET, preclinical, collimator, high energy, high sensitivity, Monte Carlo

Supplementary material for this article is available online

Abstract

Objective. Clustered pinhole (CP) collimation currently supports sub-millimeter resolution imaging up to ∼1 MeV, enabling SPECT of alpha and beta emitters with gamma emissions, simultaneous multi-isotope PET and PET/SPECT, and positron range-free PET. Nonetheless, increasing sensitivity in the original CP designs by enlarging pinhole diameters is limited, as the resulting pinhole opening cones would overlap. *Approach.* To address this limitation, the use of Super-Cluster (SC) collimation was evaluated in a simulation study. Two SC designs were assessed: a standard configuration (SC-ST) offering a resolution-sensitivity trade-off similar to CP, and a high-sensitivity variant (SC-HS) with larger pinhole diameters to enhance sensitivity. Their performance was compared to CP collimation for ^{18}F at concentrations of 1.0, 0.1, 0.05 MBq ml^{-1} and ^{89}Zr at 2.0, 0.2, 0.1 MBq ml^{-1}, evaluating sensitivity, image resolution, recovery coefficients, and uniformity. *Main results.* CP and SC-ST showed comparable sensitivity and image resolution. Both resolved ^{18}F rods of 0.9, 1.4, and 1.8 mm at 1.0, 0.1, and 0.05 MBq ml^{-1}, respectively. For ^{89}Zr, rods down to 1.0 mm and 1.6 mm were resolved at 2.0 and 0.2 MBq ml^{-1}, but none at 0.1 MBq ml^{-1}. Compared to CP and SC-ST, SC-HS increased sensitivity threefold for ^{18}F and twofold for ^{89}Zr. At the highest activity, SC-HS showed slightly reduced resolution for ^{18}F (1.0 mm) and similar for ^{89}Zr (1.0 mm). However, it clearly outperformed both other collimators at lower activities, resolving ^{18}F rods of 1.2 and 1.4 mm at 0.1 and 0.05 MBq ml^{-1}, respectively, and ^{89}Zr rods of 1.4 and 1.6 mm at 0.2 and 0.1 MBq ml^{-1}. Additionally, SC-HS showed superior contrast recovery. Image uniformity remained consistent across all collimators, confirming effective angular sampling. *Significance.* The new SC geometry enables high-sensitivity collimation for high gamma energies, improving image quality at low activities. These results demonstrate SC collimation's strong potential for sensitivity-critical applications.

1. Introduction

State-of-the-art preclinical SPECT plays a pivotal role in advancing basic research and developing new diagnostic and therapeutic applications (Franc *et al* 2008, Rowland and Cherry 2008, Bernsen *et al* 2014). It provides invaluable insight into biological processes as it enables *in vivo* imaging and quantification of radiotracer biodistribution with spatial resolutions down to a quarter of a millimeter (Ivashchenko *et al* 2014). To achieve such high spatial resolution (where higher spatial resolution refers to the visibility of smaller structures, i.e. smaller FWHM values), these SPECT systems commonly use multi-pinhole collimators (Wouters *et al* 1973) combined with high image magnification to significantly reduce the impact of limited detector intrinsic resolution (Beekman and van der Have 2007).

Although offering promising performance, earlier SPECT systems had limited applicability, as they were typically designed to operate within the gamma energy range of approximately 25–350 keV, which encompasses several commonly used radionuclides, such as ^{125}I (27–35 keV), ^{99m}Tc (140 keV), ^{111}In (171 and 245 keV), ^{201}Tl (69–83 and 167 keV), and ^{67}Ga (93–300 keV). While higher-energy emitters such as ^{131}I (364 keV) could in principle be imaged with conventional SPECT systems, the resulting image quality and resolution were generally suboptimal. In response to this limitation, over the past decade our group, in collaboration with the company MILabs B.V., has worked to significantly extend the maximum gamma energy (Goorden and Beekman 2010). These efforts culminated in the development of the VECTor (Versatile Emission Computed Tomography) scanner (Goorden *et al* 2013), which has demonstrated sub-millimeter resolution for both SPECT and PET imaging at energies up to 1 MeV in experimental studies (Beekman *et al* 2021), and recently has been investigated through simulations for even higher energies (Ghosh *et al* 2025). This high-energy performance was enabled by the integration of clustered pinhole (CP) technology into the system (Beekman 2011).

The capabilities of CP collimation have sparked growing interest in imaging radionuclides with complex spectra and/or high-energy gamma emissions (Esquinas *et al* 2017, Robertson *et al* 2017, Koniar *et al* 2024). For instance, accurate determination of the biodistribution of ^{209} At, which together with ^{211}At forms a promising theranostic pair for targeted alpha therapy, has been demonstrated with high spatial and temporal resolution (Crawford *et al* 2018, Ogawa *et al* 2021). For ^{213}Bi and ^{131}I, both important for existing and emerging therapeutic approaches, image resolutions of 0.75 mm and 0.60 mm have been achieved using their 440 keV and 364 keV gamma emissions, respectively (de Swart *et al* 2016, van der Have *et al* 2016). In addition to imaging therapeutic radionuclides, VECTor can also utilize prompt gamma emissions from positron-emitting nuclei, effectively eliminating blurring caused by positron range. The use of these prompt gammas resulted in image resolutions of 0.75 mm for ^{89}Zr and ^{124}I, based on their 909 keV and 603 keV emissions, respectively (Beekman *et al* 2021), and enabled the development of many new multi-isotope PET protocols.

While these high-resolution imaging results are promising, translating this performance to a broader range of theranostic isotopes remains challenging. Many of these isotopes are characterized by high-energy emissions and low administered activity, requiring collimators that combine effective high-energy performance with higher sensitivity than current CP designs provide to ensure high-quality images. Additionally, enhanced sensitivity reduces statistical noise and enables *in vivo* imaging at lower activity levels or at shorter scan times, which in turn facilitates the development of new tracers, lowers isotope costs and allows for faster dynamic imaging, making it possible to capture rapid biological processes (Sigurdsson *et al* 2023).

A straightforward approach to achieve higher sensitivity is to enlarge the size of the pinhole apertures, modulating the resolution-sensitivity trade-off. In a previous work we developed and validated an ultra-high-sensitivity collimator with 2.0 mm conical pinholes that achieved a 1.3% peak sensitivity for ^{99m}Tc while maintaining sub-millimeter resolution (Ivashchenko *et al* 2015). However, this design was optimized for standard SPECT isotopes with typical low energy gamma emissions (<350 keV (Saeedi Saghez *et al* 2024, Wharton *et al* 2024)) and is not suitable for higher-energy applications for which CP technology is required. Nonetheless, as we demonstrate in this work, the clustered configuration of CP introduces geometrical constraints that limit design flexibility. In particular, enlarging the pinhole diameter in this design causes significant overlap between pinhole cones, increasing the chance of unwanted collimator penetration.

To overcome this challenge and enhance sensitivity for high-energy imaging, a Super-Cluster (SC) geometry was introduced (Beekman 2022). Similar to CP collimation, the SC design uses small opening-angle pinholes to reduce edge penetration. However, it samples the same central area (central field-of-view, CFOV) through a fundamentally different pinhole arrangement. In each ring, the pinholes are arranged in a fan-like pattern with offsets between them, forming what is known as a SC. This results in a more uniform pinhole distribution across the collimator surface compared to the CP approach. SC collimators currently offer a range of resolution–sensitivity trade-offs, with the ultra-high sensitivity version (ultra-HS) achieving up to 17.0% sensitivity for ^{18}F when paired with a 19 mm thick scintillation crystal (Nguyen *et al* 2022, MILabs 2024).

This paper for the first time presents the underlying principles of the SC geometry (Beekman 2022) in detail and evaluates its performance against conventional CP collimation. To this end, a simulation approach was chosen, as it enables a controlled comparison between the two designs. Accordingly, two SC-based collimators were designed and assessed using Monte Carlo (MC) simulations. The first design, termed '*SC Standard*,' maintains the same resolution-sensitivity trade-off as CP and was developed to confirm that the SC sampling approach does not introduce artifacts. The second design, '*SC High-Sensitivity*,' demonstrates how the SC geometry can easily achieve higher sensitivity through a simple

increase in pinhole diameter. Sensitivity, image resolution, recovery coefficient (RC), and uniformity were evaluated for both collimator types using two commonly employed positron-emitting radiotracers in nuclear medicine, ^{18}F (Reivich *et al* 1979, Vallabhajosula 2007, Alauddin 2012) and ^{89}Zr (Borjesson *et al* 2006, Vosjan *et al* 2010, De Feo *et al* 2022), at different activity concentrations.

2. Materials and methods

2.1. Imaging system

Collimators in this MC simulation study were modeled as part of a VECTor imaging system (Goorden *et al* 2013), which features three PMT-based large-area monolithic NaI(Tl) scintillation detectors, each measuring 590 × 470 × 9.5 mm^3, arranged in a stationary triangular layout.

Existing collimators used on this SPECT-PET system feature focusing pinhole geometries, where the pinholes sample a common CFOV, ensuring that complete data can be obtained within this region. This design enables imaging of objects or organs within the CFOV without requiring movement of the object. For larger subjects, such as whole-body animal scans, bed translation is required to grant adequate sampling. Images are then reconstructed using projection data from all bed positions belonging to one time frame simultaneously (Vastenhouw and Beekman 2007).

For standard pinhole collimators, data completeness within the CFOV is achieved by ensuring that each pinhole in the cylindrical collimator covers a FOV that always includes the entire CFOV. For CP, each cluster of four pinholes rather than every individual pinhole views the CFOV, as explained in section 2.1.1. For the SC collimators, an alternative sampling strategy was adopted as detailed in section 2.1.2.

2.1.1. CP collimator design and geometrical constraints

The CP collimator simulated is modeled closely after the existing experimental collimator. It is constructed from a rather easily machinable tungsten alloy containing 97.0% tungsten, 1.5% nickel, and 1.5% iron (alloy density 18.5 g cm^{-3}) with a cylindrical shape and inner and outer radii of 24 mm and 67 mm, respectively (Goorden and Beekman 2010). This design's wall thickness ensures that only 0.005% of 511 keV gammas and 0.3% of 909 keV gammas can pass through the solid wall perpendicularly, with the probability decreasing at oblique angles due to the increased material thickness encountered. The effectiveness of this wall thickness for both 511 keV and 909 keV gammas has also been experimentally demonstrated (Goorden *et al* 2013, Beekman *et al* 2021).

The pinholes are asymmetrically located within the collimator wall (a cylindrical shell with inner radius of 24 mm and outer radius of 67 mm); they are offset toward the inner surface, with their centers at a radius of 32 mm. This setup enables significant pinhole magnification factors while still employing the thick collimator walls necessary for high-energy gamma imaging. High pinhole magnification is crucial for achieving high-resolution imaging, as it offsets the limited intrinsic resolution of the gamma detector, which is ∼3.5 mm in this case. The pinholes, each measuring 0.7 mm in diameter, are organized into 48 clusters of 2 by 2 individual pinholes distributed across four rings. Of the total 192 pinholes, 162 are used for image reconstruction, while the remaining are excluded because their projections fall into the gaps between the three detectors. Each cluster is designed to sample the same FOV as a traditional pinhole, while incorporating narrower individual pinhole opening angles (POA) of 18° in the inner rings and 16° in the outer rings to reduce edge penetration effects that degrade image resolution (van der Have *et al* 2009, Goorden and Beekman 2010, Beekman 2011). These angles also ensure a good fit of the elliptical pinhole projections over the detector surface (Mok *et al* 2009).

For traditional pinholes, adjusting their diameter offers a straightforward way to modulate the resolution-sensitivity trade-off. In contrast, CP offers less flexibility in this regard, as the close spacing of pinholes within each cluster limits diameter increases, since larger sizes lead to overlapping pinhole cones (figures 1(a) and (b)).

2.1.2. SC collimator design

To address this limitation, the SC collimator uses an alternative geometry which will be described here. In this design, each ring comprises two sub-rings of evenly spaced pinholes.

As in CP design, a single pinhole cannot fully sample the CFOV due to the narrow POA. Instead, complete sampling of the elliptical CFOV is achieved by each full sub-ring, where pinholes are arranged in a fan-like pattern and collectively form a unified SC (Beekman 2022). To enable this full coverage, each pinhole in a sub-ring is offset in the same direction and oriented to view a specific portion of the CFOV, with its sampled region illustrated by a projection cone shown as a shaded area in figures 1(c) and (d). This offset configuration ensures that each projection covers a neighboring but distinct area of

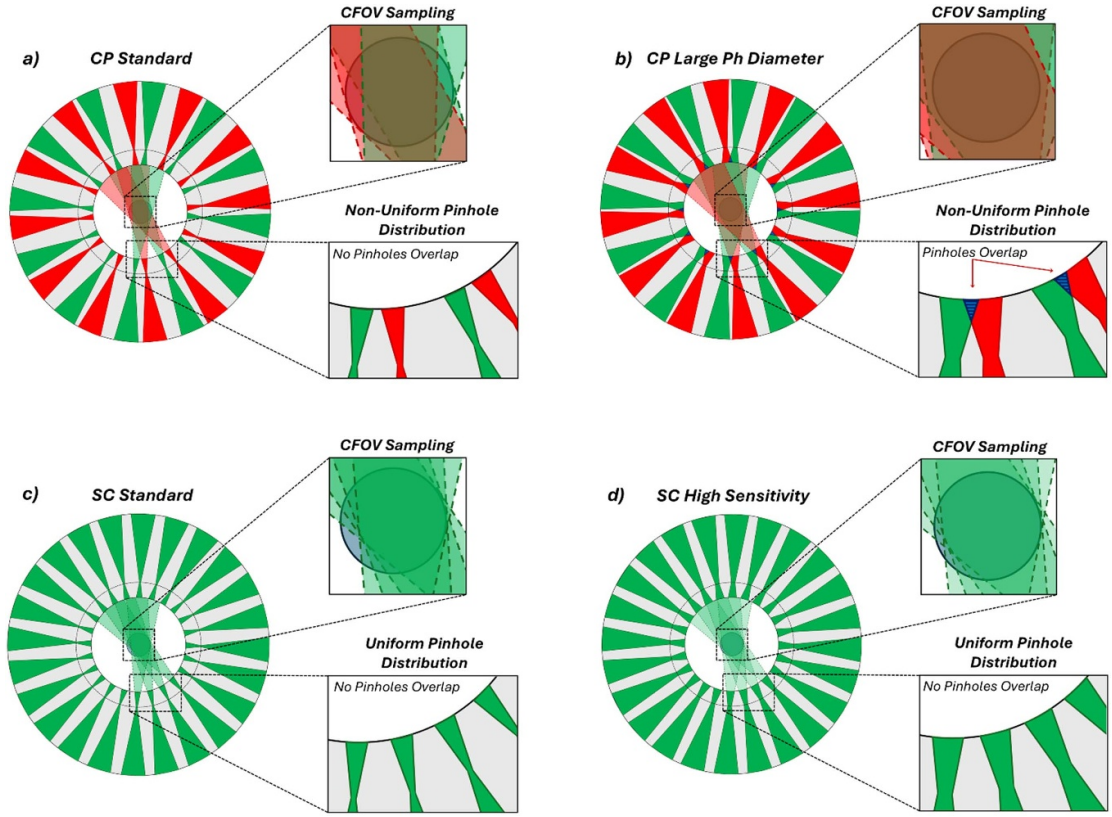

Figure 1. Illustration of CP (top) and SC (bottom) collimator ring geometries. Panels show the sampling of the CFOV (light blue circle) and the pinhole distributions. In CP configuration (a) and (b), within a ring pinholes are arranged less regularly due to the clustered design: pinholes within a cluster are closely spaced, while those from different clusters are more widely separated. This arrangement can lead to physical overlap when the pinhole diameter is increased, for example from 0.7 mm (a) to 2.0 mm (b). Such large pinhole-diameter CP configurations are not implemented in practice, as the resulting overlap would cause excessive collimator penetration, making them impractical. In contrast, the SC configuration (c) and (d) features a more uniform layout, with all pinholes evenly spaced. This regularity allows for an increase in pinhole diameter, in this case from 0.7 mm (c) to 2.0 mm (d), without encountering geometric constraints w.r.t. cone overlap.

the CFOV. As a result, moving counterclockwise along the sub-ring, the right-hand edge of each pinhole's coverage is progressively surpassed by that of the next, gradually expanding the overall sampled area of the CFOV. This systematic offset continues until the combined pinhole projections completely cover the CFOV. The second sub-ring follows the same principle, with its pinholes offset progressively expanding the sampled area of the CFOV when moving clockwise along the sub-ring (figure 2).

This design offers a straightforward solution to the limitations of CP collimator encountered when increasing pinhole diameter, providing a simpler and more flexible configuration with pinholes more evenly distributed across the collimator surface. Moreover, it is capable of maintaining narrow POA, such as those used in CP, which are necessary to minimize edge penetration effects.

Although the overall geometry differs substantially, several parameters were kept consistent with CP collimators to ensure a fair comparison and enable identical imaging studies that isolate the impact of the new design. Specifically, the material composition, CFOV size, degree of pinhole multiplexing on the detector, the inner and outer radii of the collimator, and the radius at which the pinhole centers were placed in the collimator wall were maintained. Adjustments were made to the number of pinholes, their opening angles and diameters, to achieve the desired performance.

Building on this controlled comparison, two distinct SC collimator designs were developed to explore different aspects of its performance. A first design, termed '*SC Standard*' (SC-ST), was made using the same pinhole diameter and POAs as CP collimator, aiming for a similar resolution-sensitivity trade-off. This design was used to verify that the SC sampling method does not introduce artifacts compared to CP and to assess the impact of the new pinhole geometry on system performance. A second design, referred to as '*SC High Sensitivity*' (SC-HS), was made to prioritize sensitivity by employing larger pinhole diameters than CP. To limit the associated resolution loss, the diameter was set to 2.0 mm, providing a balance between sensitivity improvement and modest degradation in resolution. This design also

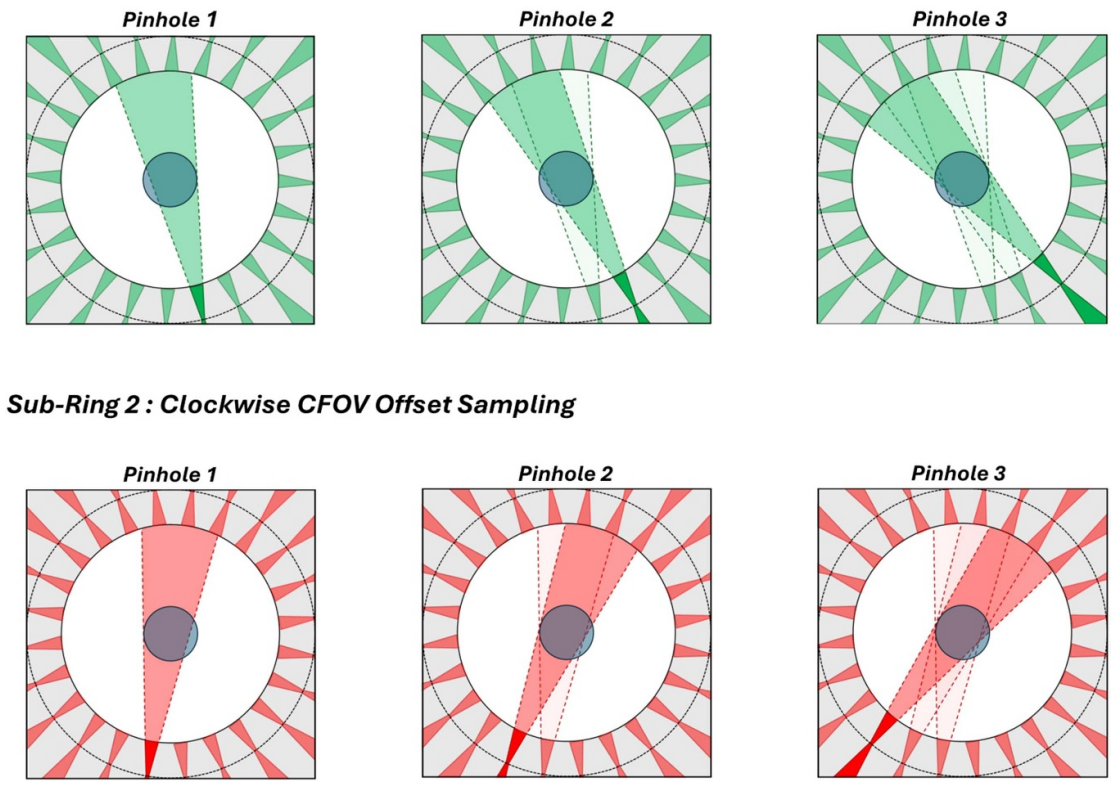

Figure 2. Illustration of the opposing orientation of pinholes in adjacent rings within the SC configuration. The sampling of the CFOV (light blue circle), both individually and collectively achieved by the pinholes, is shown through their shaded projection cones.

incorporates smaller POAs compared to CP, enabled by the larger pinhole diameter, which increases the sampled FOV. The POAs were set to the minimum values required to maintain the same sampled FOV as the CP while ensuring complete axial sampling and adequate coverage of the elliptical pinhole projections across the detector surface.

2.1.3. Pinhole arrangement in SC collimator

The pinhole centers in each sub-ring were positioned midway between the centers of adjacent pinholes in neighboring sub-rings, ensuring an even distribution of pinholes both within each sub-ring and across the entire ring. The z-coordinates of the pinholes' centers were determined through an iterative process. This involved adjusting the distances between sub-rings and rings along the z-direction, while evaluating how the resulting geometric pinhole projections covered the detector surface and assessing the extent of multiplexing among them. The latter was calculated by verifying whether each detector pixel center was within a detector area covered by single or multiple pinholes projection cones.

$$\text{Multiplexing } [\%] = 100 * \frac{\#\text{ pixels within multiple cones}}{\#\text{ pixels with non - zero value}}. \quad (1)$$

The values chosen for our final designs were those that, in combination with the selected POA, provided optimal detector coverage and a multiplexing as close as possible to that of the CP (29.3%).

2.2. Simulation setup and data acquisition process

In our study, we compared the two SC collimators to the traditional CP collimator. To perform this comparison, we generated data using MC simulations with GATE v9.0, based on Geant4 version 10.05 (GATE users guide). These simulations modeled gamma photon interactions with the detector while omitting the tracking of their optical transport, including bulk and boundary processes. The behavior of gamma photons was defined through GATE's '*emstandard*' list of standard electromagnetic processes. The imaging system and phantoms were modeled using GATE primitives (i.e. cylinder, boxes and cones). An image of the resulting system model is provided in the appendix (figure A1).

The simulations were conducted assuming the imaging system was equipped with either the SC or CP collimator. The detector performance was based on manufacturer specifications, including an intrinsic spatial resolution of 3.5 mm and energy resolutions of 9.0% for 511 keV photons and 6.7% for 909 keV photons. Interaction events within the detector were simulated by introducing random variations in energy and position, sampled from Gaussian distributions with standard deviations (σ) calculated from the reported resolutions. Natural background was included in the simulation to better reflect real system behavior. A background factor per detector pixel was calculated using the manufacturer-provided background count rate (81 counts per second for ^{18}F and 63 counts per second for ^{89}Zr within the photopeak window), combined with the photopeak window width and scan duration defined in this study. This factor was used to generate Poisson-distributed natural background counts added to the data.

These simulations were utilized to measure sensitivity, as well as to generate forward projections for resolution, recovery, and uniformity phantoms which will be covered in the following sections.

2.2.1. Sensitivity phantom

Sensitivity was assessed by evaluating both the peak value and the CFOV-averaged value. The peak sensitivity was determined by simulating a spherical source in air (0.1 mm radius) positioned at the center of the collimator. The CFOV-averaged sensitivity was obtained using an ellipsoidal source in air matching the CFOV dimensions ($12 \times 12 \times 9$ mm^3 axes). The phantoms were filled with either ^{18}F or ^{89}Zr at concentrations of 2.0 MBq ml^{-1} and scanned for one hour.

2.2.2. Resolution phantom

Image resolution was evaluated using a Derenzo phantom made of PMMA, shaped as a cylinder with a diameter of 24 mm and a height of 12 mm. Given the wide range of activity concentrations analyzed and the six-sector design of a typical resolution phantom, we used two distinct versions. The first contained rods with diameters of 1.2 mm, 1.1 mm, 1.0 mm, 0.9 mm, 0.8 mm, and 0.7 mm, while the second had rods measuring 1.8 mm, 1.6 mm, 1.4 mm, 1.2 mm, 1.1 mm, and 1.0 mm (figure 3). Each rod was 8 mm in height, with a center-to-center spacing within each sector equal to twice the rod diameter. To account for the system's varying detection capabilities, the rods were filled with different concentrations of ^{18}F and ^{89}Zr. For ^{18}F, the resolution phantom with smaller rods was filled with 1.0 MBq ml^{-1}, while the phantom with larger rods used concentrations of 0.1 MBq ml^{-1} and 0.05 MBq ml^{-1}. For ^{89}Zr, the smaller-rod phantom was filled with 2.0 MBq ml^{-1}, and the larger-rod phantom with 0.2 MBq ml $^{-1}$ and 0.1 MBq ml^{-1}. These phantoms were scanned for one hour across nine bed positions. These positions were arranged in a 3×3 grid, with adjacent points spaced 6 mm apart in the transaxial plane, while only a single axial position was used. Considering the size of the CFOV and of the phantom (a cylinder with a 20 mm diameter and 10 mm height), this represents a conservatively high number of bed positions. This approach was chosen to grant comprehensive sampling of the object (figure 3), ensuring that every part of the scan volume was covered by the CFOV at least once.

2.2.3. Calibration point source

The calibration factor is defined as the ratio of the activity concentration to the voxel value in reconstructed SPECT images (Wu *et al* 2010). For each collimator, these factors were determined by simulating a spherical point-like source with a 1.5 mm radius, filled with a known activity of ^{18}F or ^{89}Zr. The source was positioned at the collimator's center and scanned for 1 h.

2.2.4. RC phantom

The RC was evaluated using a cylindrical PMMA phantom (20 mm in diameter, 10 mm in height) containing five rods with diameters of 2.5 mm, 2.0 mm, 1.5 mm, 1.0 mm, and 0.5 mm, each 6.5 mm in height. The rods were uniformly filled with either ^{18}F at concentrations of 1.0 MBq ml^{-1}, 0.1 MBq ml^{-1}, or 0.05 MBq ml^{-1}, or with ^{89}Zr at concentrations of 2.0 MBq ml^{-1}, 0.2 MBq ml^{-1}, or 0.1 MBq ml^{-1}. This phantom design is based on the sector of the NEMA image quality phantom (N.E.M. Association 2008) used to assess RC. The size and activity concentration of the original NEMA phantom were adjusted to meet our goal of analyzing performance of a high-resolution preclinical SPECT system at low activity concentration levels (Visser *et al* 2011). The scan sequence comprised the same nine bed positions as for the Derenzo phantom, with a total scan duration of 1 h.

2.2.5. Uniformity phantom

Uniformity was evaluated using a cylindrical PMMA phantom (18 mm in diameter, 10 mm in height) containing a cylindrical central cavity (14 mm in diameter, 6 mm in height) uniformly filled with either

^{18}F at concentrations of 10 MBq ml^{-1}, 1.0 MBq ml^{-1}, 0.1 MBq ml^{-1}, and 0.05 MBq ml^{-1} or ^{89}Zr at 20 MBq ml^{-1}, 2.0 MBq ml^{-1}, 0.2 MBq ml^{-1}, and 0.1 MBq ml^{-1}. The highest activity concentrations (10 MBq ml^{-1} for ^{18}F and 20 MBq ml^{-1} for ^{89}Zr) were included to specifically assess the potential emergence of design-related artifacts under high-statistics conditions. The corresponding results are shown in the appendix (figure A3). The scan sequence included 21 bed position, following a spiral trajectory (Vaissier *et al* 2012) along the phantom to ensure optimal axial sampling, with a total scan time of 1 h.

2.3. Image reconstruction

The image reconstruction process started with defining energy acceptance windows for both the photopeak and the triple-energy window scatter correction technique (Ogawa *et al* 1991). A 20% energy window was centered on the 511 keV photopeak for ^{18}F and the 909 keV photopeak for ^{89}Zr. For scatter correction, two additional side windows were positioned adjacent to the photopeak, each set to 25% of the main photopeak window's width.

System matrices were created for every collimator and radionuclide evaluated in our study. We utilized a ray-tracing technique to calculate these matrices, which considers energy dependent attenuation within the collimator and detector while it ignores scatter (Goorden *et al* 2016).

Images were reconstructed via the dual-matrix dual-voxel (DM-DV) pixel-based similarity-regulated ordered subsets expectation maximization (SROSEM) method (Goorden *et al* 2020). The DM-DV approach enhances computational efficiency by employing two voxel sizes: smaller voxels for the central region of the point spread function (PSF) and larger voxels for its slowly varying tails. The central PSF area, extending to 20% of its peak value, was modeled with 0.4 mm voxels, while the peripheral tails were modeled with 0.8 mm voxels. During backprojection, only the central portion of the PSFs was considered. This photon transport modeling was integrated with the SROSEM algorithm, which adapts the number of subsets automatically and locally, up to a maximum of 128 (Vaissier *et al* 2016).

Post-processing consisted in applying 3D Gaussian filters with varying FWHMs, with specific values provided in the captions of the corresponding images.

2.4. Data analysis

Data from the sensitivity, resolution, recovery, and uniformity phantom studies were used to quantitatively evaluate the SC and CP collimators' performance.

Peak and average sensitivity were measured using data from the sensitivity phantoms and were defined as the ratio between the number of photons detected per decay and the total emissions, where the latter refers to the number of emitted positrons for ^{18}F and the number of emitted prompt gammas for ^{89}Zr:

$$\text{Sensitivity } [\%] = 100 * \frac{\#\text{detected photons per decay}}{\#\text{emissions}}. \tag{2}$$

This calculation was performed by applying an energy acceptance window from 150 keV to 650 keV, based on the NEMA protocol (N.E.M. Association 2008). For ^{89}Zr, a similar approach was applied, with an acceptance window ranging from 150 keV to 1100 keV. Additionally, sensitivity was calculated in cps/MBq, taking into account the branching ratio of the emission responsible for the detected photons for ^{18}F and ^{89}Zr (96.7% and 99.0% respectively). A contrast-to-noise ratio (CNR) analysis was conducted on the unfiltered reconstructed images of the resolution phantom (Walker *et al* 2014). For this purpose, the images were resampled onto a fine grid, and circular regions of interest (ROIs) were positioned over the rods and the surrounding areas (figures 3 and 4). The ROIs had diameters equal to 90% of the corresponding rod size and were placed across 10 consecutive 0.4 mm slices of the reconstructed images. By determining the activity in each ROI, we calculated the contrast (C) in each sector (i) with the following equation:

$$C_{\text{rods},i} = \frac{\bar{h}_i - \bar{c}_i}{\bar{h}_i}. \tag{3}$$

Here $\bar{h}_i$ and $\bar{c}_i$ are respectively the mean activity in all ROIs placed on and between the rods in sector i. Furthermore, the noise in each sector (N_i) was calculated:

$$N_{\text{rods},i} = \frac{\sqrt{\sigma_{h,i}^2 + \sigma_{c,i}^2}}{\bar{h}_i + \bar{c}_i}. \tag{4}$$

Table 1. Peak and CFOV-averaged sensitivities for ^{18}F and ^{89}Zr using CP, SC standard (SC-ST), and SC high sensitivity (SC-HS) collimators with a thin (9.5 mm) crystal. Results for ^{18}F were calculated for an energy window going from 150 keV to 650 keV, while for ^{89}Zr for an energy window going from 150 keV to 1100 keV.

	^{18}F		^{89}Zr	
Collimator	Peak sensitivity (cps/MBq) (%)	CFOV sensitivity (cps/MBq) (%)	Peak sensitivity (cps/MBq) (%)	CFOV sensitivity (cps/MBq) (%)
CP	3.6 * 10^3 (0.70%)	2.8 * 10^3 (0.55%)	8.1 * 10^3 (0.82%)	7.3 * 10^3 (0.74%)
SC-ST	3.8 * 10^3 (0.74%)	3.0 * 10^3 (0.58%)	8.4 * 10^3 (0.85%)	7.5 * 10^3 (0.76%)
SC-HS	1.1 * 10^4 (2.1%)	8.8 * 10^3 (1.7%)	1.6 * 10^4 (1.6%)	1.4 * 10^4 (1.4%)

Here $\sigma_{h,i}$ and $\sigma_{c,i}$ are respectively the standard deviation of the activity in ROIs on and in between rods. Using (3) and (4), the average CNR over five runs was calculated and plotted against the iteration number.

To determine the RC values from the recovery phantom, the calibration factors (CF) for each collimator were first evaluated. The CF were defined as (Wu *et al* 2011):

$$\mathrm{CF}\left[\frac{\mathrm{MBq}}{\mathrm{ml}}\right] = \frac{A}{V * \sum R}. \tag{5}$$

Here A represents the activity in MBq of the source used in the simulation, $\sum R$ is the summation of all voxel values in the reconstructed SPECT image, and V is the volume of a voxel in ml. These CFs were then applied to convert the reconstructed voxel values into activity concentrations. The RCs for the filled rods were calculated by defining ROIs with diameters equal to 90% of the corresponding rod sizes. The ratio of the estimated concentration from the SPECT reconstructed image (C_{SPECT}) within the selected ROI to the true concentration used in the simulation (C_{True}) for the corresponding rod was then calculated:

$$\mathrm{RC}\ [\%] = 100 * \frac{C_{\mathrm{SPECT}}}{C_{\mathrm{True}}}. \tag{6}$$

The average RCs for each rod, calculated over five runs, are reported in tables for all the collimators.

Image uniformity was quantitatively evaluated by calculating the percentage uniformity. Six circular ROIs with a diameter of 3.0 mm were placed at five consecutive axial positions, evenly spaced at 0.8 mm intervals, on the reconstructed unfiltered uniformity phantom images (Walker *et al* 2014). The average value within the ROIs and the standard deviation between them, $\bar{U}$ and σ_{U} respectively, were measured to quantify the percentage uniformity.

$$\mathrm{Uniformity}\ [\%] = 100 * \frac{\sigma_{\mathrm{U}}}{\bar{U}}. \tag{7}$$

For all the configurations analyzed, the average percentage uniformity calculated over three simulation runs of the same setup were reported in tables A1 and A2 in the appendix.

3. Results

3.1. SC collimator designs

Two SC designs were obtained as described below.

The SC-ST features 192 0.7 mm diameter pinholes (165 used for reconstruction) arranged in four rings. The pinhole centers of the two innermost rings were at 32.2 mm for the first sub-ring and 33.7 mm for the second sub-ring from the collimator center, while for the two outermost rings they were at 36.8 mm for the first sub-ring and 41.1 mm for the second sub-ring. The POAs were 18° and 16° respectively for the two innermost, and two outermost rings.

The SC-HS design consists of 192 pinholes (159 used for reconstruction), each with a diameter of 2.0 mm, arranged in four rings. The POAs are 15° for the innermost rings and 13° for the outermost rings. In this design, the pinhole centers were positioned at 32.2 mm and 33.8 mm from the collimator center for the first and second sub-ring of the innermost rings, respectively, and at 36.6 mm and 41.7 mm for the first and second sub-ring of the outermost rings.

In terms of multiplexing, the SC-ST and SC-HS designs achieved values of 29.4% and 29.1%, respectively, which are comparable to the 29.3% achieved by the CP collimator.

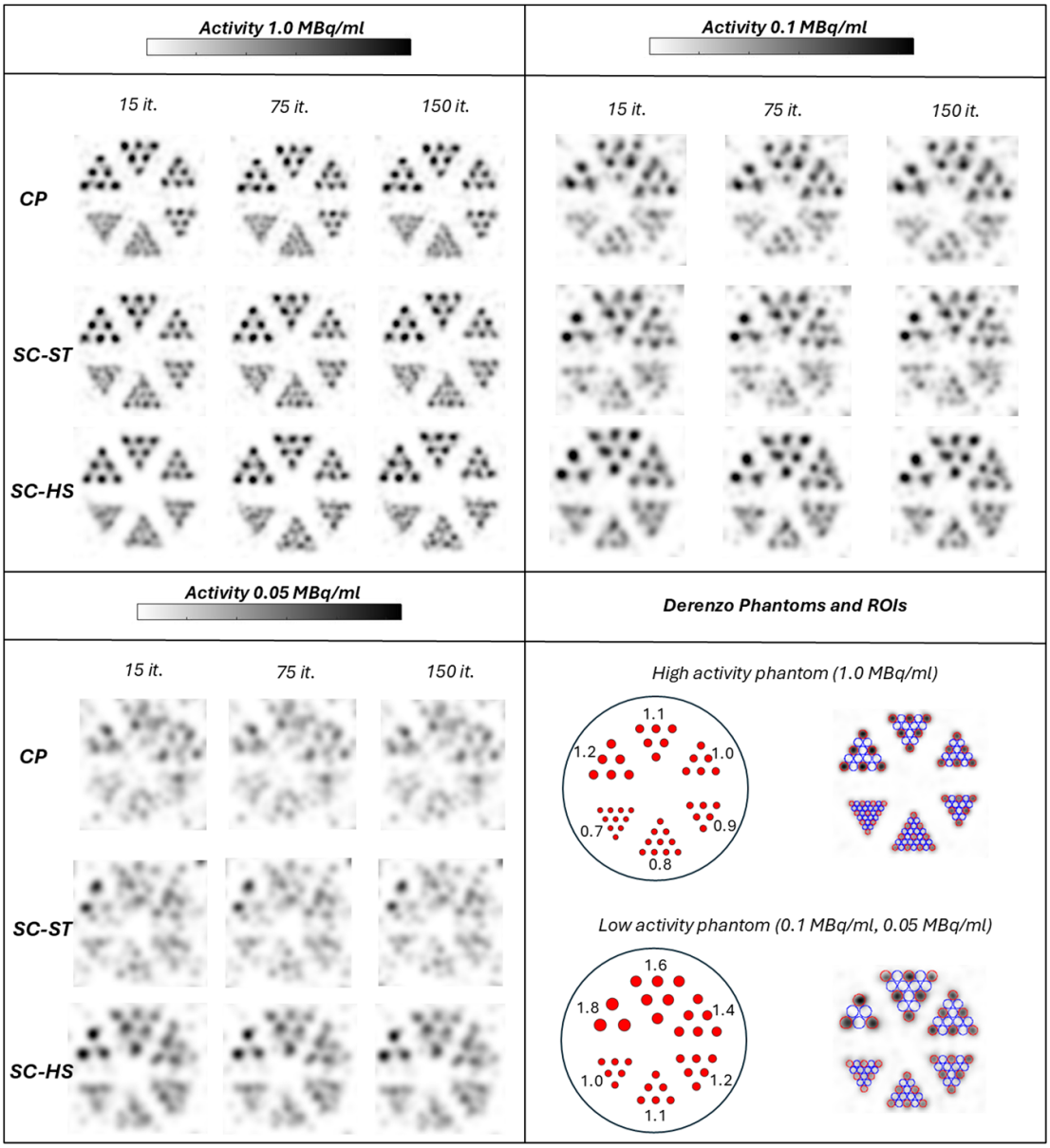

Figure 3. Resolution phantom images acquired using the CP and SC collimators for ^{18}F. For 1.0 MBq ml^{-1} activity concentration, rods with diameters of 1.2 mm, 1.1 mm, 1.0 mm, 0.9 mm, 0.8 mm, and 0.7 mm were used. For the remaining activity concentrations, the rod diameters were 1.8 mm, 1.6 mm, 1.4 mm, 1.2 mm, 1.1 mm, and 1.0 mm. A 3D Gaussian filter with a 0.8 mm FWHM was applied to images acquired at 1.0 MBq ml^{-1}, while FWHMs of 1.2 mm and 1.4 mm were used for images at 0.1 MBq ml^{-1} and 0.05 MBq ml^{-1} respectively. A schematic illustration of the phantom designs and of the ROIs used for the CNR analysis are also provided. The displayed images were generated by summing fifteen consecutive slices at the phantom's center, resulting in a final slice thickness of 6 mm.

3.2. Sensitivity comparison

Table 1 provides a summary of the sensitivity performance of the SC-ST and SC-HS collimators in comparison to the CP collimator.

For both isotopes, the results indicate comparable sensitivity between the CP and SC-ST collimators, while the SC-HS collimator provides approximately three times higher sensitivity for ^{18}F and two times higher for ^{89}Zr.

3.3. Image resolution comparison

Figure 3 shows reconstructed images of the resolution phantom with ^{18}F concentrations of 1.0 MBq ml^{-1}, 0.1 MBq ml^{-1}, and 0.05 MBq ml^{-1}, presented for various numbers of iterations.

Visual inspection of the image shows that at the highest tested activity concentration (1.0 MBq ml^{-1}), both CP and SC-ST can resolve 0.9 mm rods, whereas SC-HS is limited to 1.0 mm rods. At 0.1 MBq ml^{-1}, CP and SC-ST resolve rods down to 1.4 mm, while the SC-HS reaches 1.2 mm.

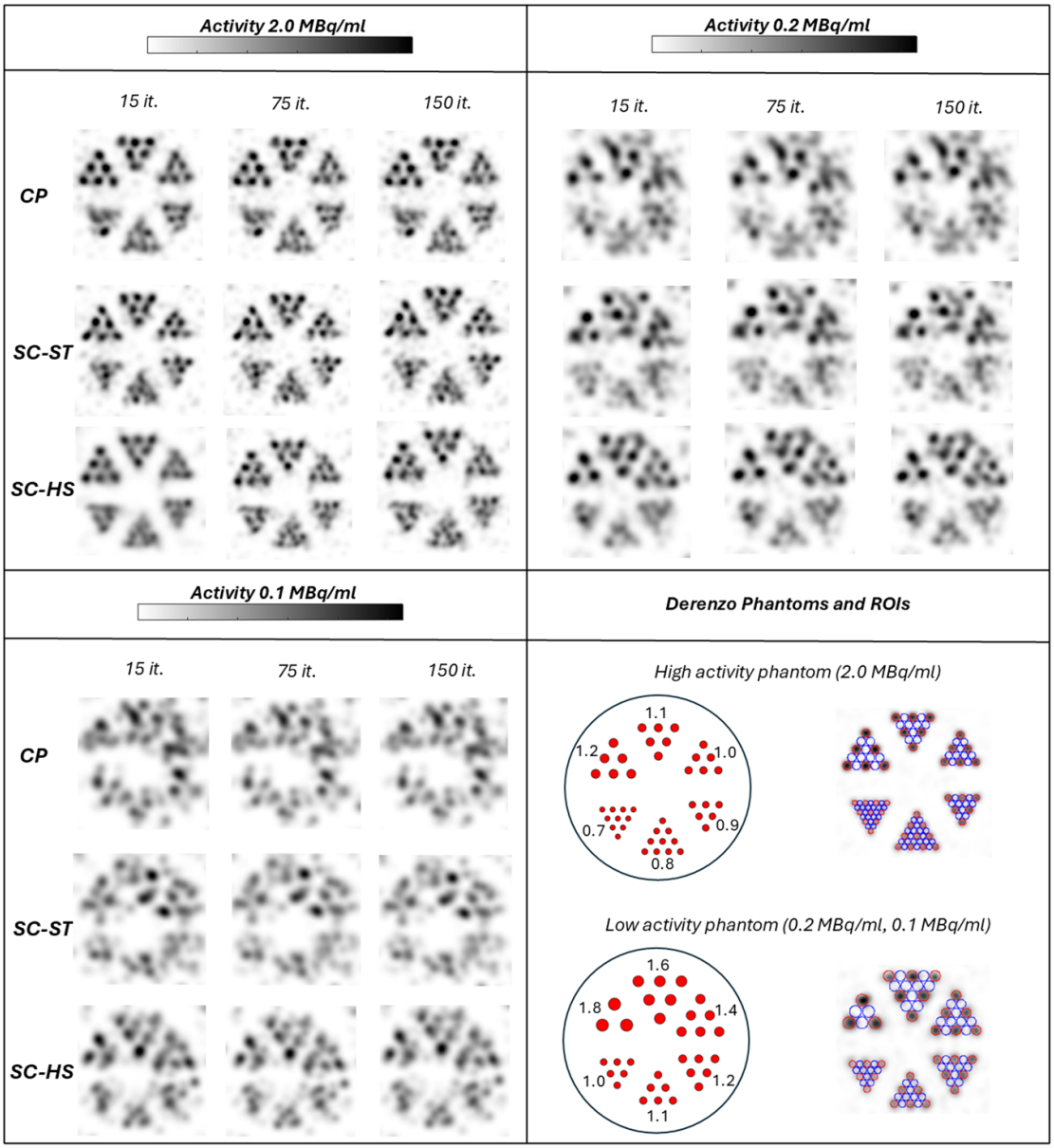

Figure 4. Resolution phantom images acquired using the CP and SC collimators for ^{89}Zr. For 2.0 MBq ml^{-1} activity concentration, rods with diameters of 1.2 mm, 1.1 mm, 1.0 mm, 0.9 mm, 0.8 mm, and 0.7 mm were used. For the remaining activity concentrations, the rod diameters were 1.8 mm, 1.6 mm, 1.4 mm, 1.2 mm, 1.1 mm, and 1.0 mm. A 3D Gaussian filter with a 0.9 mm FWHM was applied to images acquired at 2.0 MBq ml^{-1}, while FWHMs of 1.4 mm and 1.6 mm were used for images at 0.2 MBq ml^{-1} and 0.1 MBq ml^{-1} respectively. A schematic illustration of the phantom designs and of the ROIs used for the CNR analysis are also provided. The displayed images were generated by summing fifteen consecutive slices at the phantom's center, resulting in a final slice thickness of 6 mm.

Finally, at 0.05 MBq ml^{-1}, CP and SC-ST struggle to resolve any sectors, whereas SC-HS can still resolve 1.6 mm rods.

Figure 4 shows reconstructed images of the resolution phantom with ^{89}Zr activity concentrations of 2.0 MBq ml^{-1}, 0.2 MBq ml^{-1}, and 0.1 MBq ml^{-1}, presented for various iteration numbers.

At the highest activity concentration tested (2.0 MBq ml^{-1}), the performance of the three collimators is comparable as all can resolve the 1.0 mm rod sector. At 0.2 MBq ml^{-1}, both the CP and SC-ST collimators can resolve the 1.8 mm rod sector, as the 1.6 mm sector exhibits missing rods. In contrast, SC-HS successfully distinguishes rods down to 1.4 mm. At 0.1 MBq ml^{-1}, all collimators encounter difficulties: no sectors are clearly discernible with CP and SC-ST, while SC-HS still allows for visible, though slightly misplaced, identification of rods in the 1.8 mm and 1.6 mm sectors.

Line profile analyses through the smallest discernible rod sector are provided in the appendix (figure A2) for both isotopes and all activity concentrations, while corresponding analyses with ground truth are included in the supplementary material.

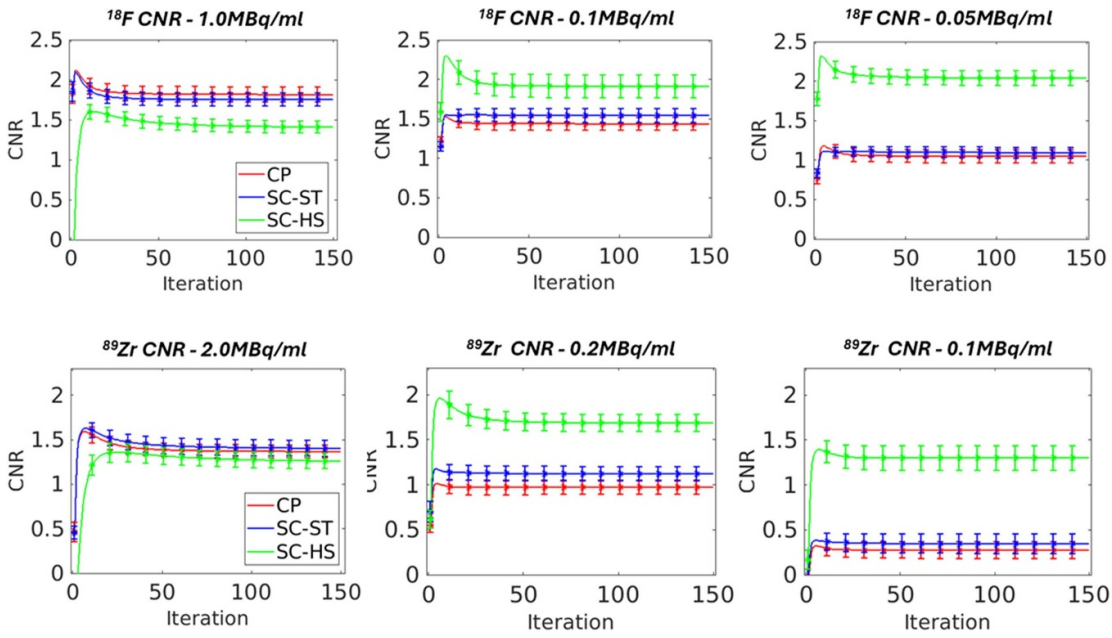

Figure 5. Mean CNR values for all tested collimators. Results, averaged across multiple runs and based on visible rod sectors and selected hot/cold regions, are plotted against the number of iterations. The images show CNR for rods filled with ^{18}F at activity concentrations of 1.0 MBq ml^{-1}, 0.1 MBq ml^{-1}, and 0.05 MBq ml^{-1}, as well as rods filled with ^{89}Zr at concentrations of 2.0 MBq ml^{-1}, 0.2 MBq ml^{-1}, and 0.1 MBq ml^{-1}.

3.4. Contrast-to-noise analysis

Beyond visual comparison, a CNR analysis was conducted on the reconstructed resolution phantom images. Figure 5 illustrates the average CNR values across all runs (considering all visible rod sectors), plotted against the number of iterations for each collimator.

For ^{18}F, at the highest activity concentration, both the CP and SC-ST collimators outperformed SC-HS by 22.1%. However, at lower activities, the SC-HS design demonstrated a significant improvement in CNR, exceeding the others by 24.0% at 0.1 MBq ml^{-1} and 85.6% at 0.05 MBq ml^{-1}. Similarly, for ^{89}Zr, the SC-HS collimator showed a moderate degradation of 10.0% at the highest activity compared to the other designs, but granted notable improvements of 33.7% at 0.2 MBq ml $^{-1}$ and 73.1% at 0.1 MBq ml^{-1}.

3.5. RCs

Images of the reconstructed recovery phantom filled with ^{18}F are shown in figure 6.

The ^{18}F RCs calculated for each rod are reported in table 2.

For ^{18}F, neither the CP nor the SC-ST design demonstrated clear overall superiority. Nonetheless, differences were observed at the lower activity concentrations (0.1 MBq ml $^{-1}$ and 0.05 MBq ml^{-1}), where the CP design outperformed SC-ST for the largest rod (2.5 mm), while SC-ST yielded better results for the smaller rods. The SC-HS design consistently achieved the best overall performance, surpassing the other collimators across all rod sizes and activity concentrations. Improvements were particularly significant at the lowest activity level, where SC-HS yielded relative gains compared to CP of 28.7%, 184.7%, and 93.3% for rods between 2.5 mm and 1.5 mm. Furthermore, for the 1.0 mm and 0.5 mm rods, the SC-HS achieved RCs of 11.4% and 5.08%, whereas the CP design yielded negligible performance.

Images of the recovery phantom filled with ^{89}Zr are shown in figure 7.

The calculated RC coefficients for ^{89}Zr are indicated in table 3.

For ^{89}Zr, performance at the highest activity concentration (2.0 MBq ml^{-1}) was comparable across all three collimators, with the SC-HS showing only a slight advantage over the CP design. As with ^{18}F, no clear preference could be established between the CP and SC-ST designs across the different activity concentrations. However, the SC-HS demonstrated superior overall results at lower activity concentrations. In particular, at the lowest tested activity (0.1 MBq ml^{-1}), SC-HS provided relative improvements over CP of 70.3%, 110.9%, and 100.0%. Additionally, SC-HS achieved an RC of 8.4% for the 1.0 mm rod while the other collimators could not recover any activity.

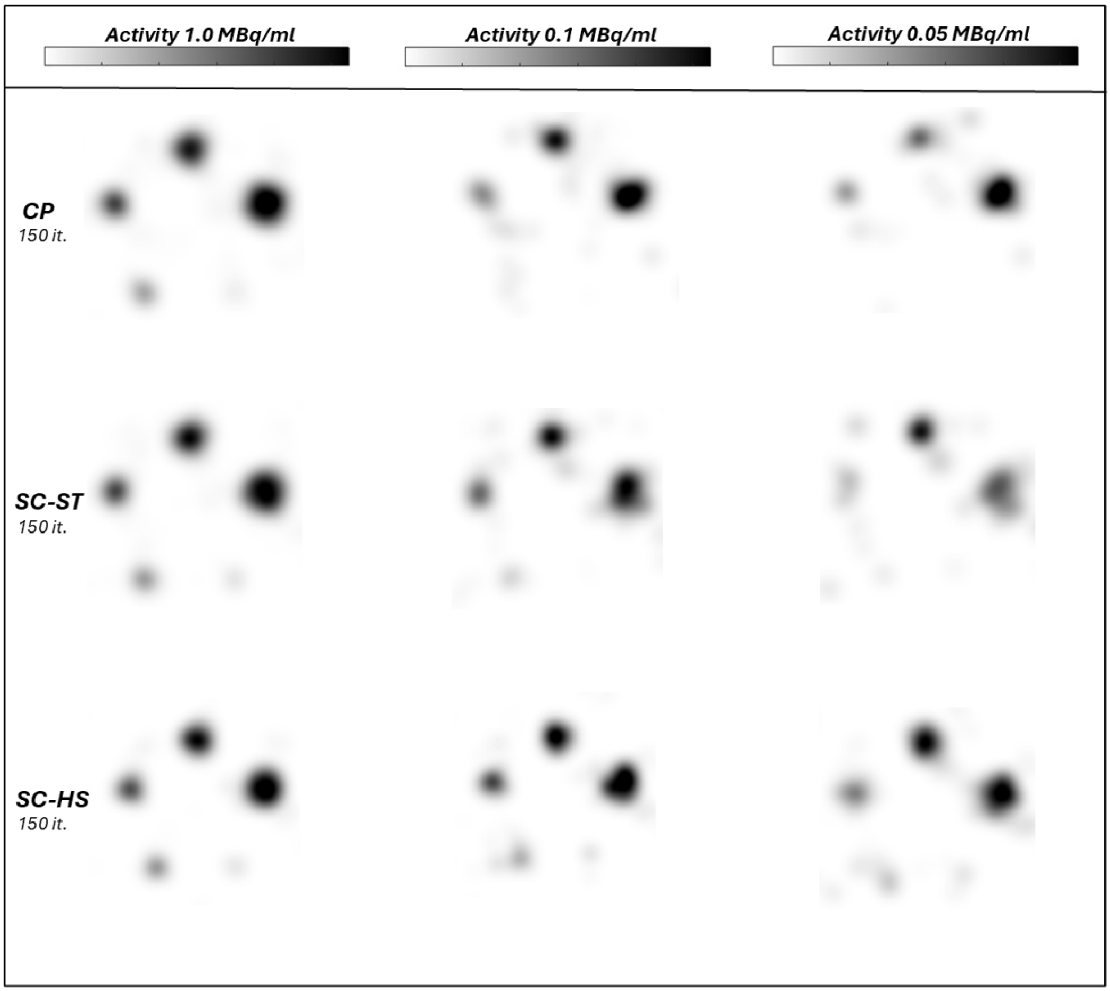

Figure 6. Images of the contrast recovery phantom imaged using CP, SC-ST, and SC-HS collimators. Rods were uniformly filled with 1.0 MBq ml^{-1}, 0.1 MBq ml^{-1}, and 0.05 MBq ml^{-1} of ^{18}F. Images shown were post-filtered with a 3D Gaussian filter having a FWHM of 1.25 mm. The displayed images were generated by summing fifteen consecutive slices at the phantom's center, resulting in a final slice thickness of 6 mm.

Table 2. Recovery coefficients (RCs), averaged over multiple runs, were calculated for all rods of the recovery phantom using both CP and SC collimators with ^{18}F. Errors represent the standard deviation across runs.

^{18}F–1.0 MBq ml^{-1}					
Collimator	RC rod 2.5 mm	RC rod 2.0 mm	RC rod 1.5 mm	RC rod 1.0 mm	RC rod 0.5 mm
CP	66.9 ± 4.1%	57.5 ± 2.5%	40.9 ± 1.4%	19.4 ± 0.9%	1.28 ± 0.3%
SC-ST	71.5 ± 4.0%	55.1 ± 1.5%	39.4 ± 0.4%	20.1 ± 0.7%	2.18 ± 0.4%
SC-HS	79.2 ± 1.1%	74.7 ± 2.3%	42.8 ± 1.2%	25.1 ± 0.1%	3.40 ± 0.3%
^{18}F–0.1 MBq ml^{-1}					
CP	67.6 ± 1.8%	46.9 ± 2.2%	25.8 ± 0.9%	3.64 ± 0.5%	$<1.0 * 10^{-6}$
SC-ST	61.0 ± 0.5%	54.4 ± 2.9%	30.1 ± 0.5%	8.22 ± 0.4%	1.02 ± 0.2%
SC-HS	73.6 ± 1.6%	70.6 ± 4.6%	36.2 ± 1.8%	20.5 ± 1.6%	5.76 ± 0.5%
^{18}F–0.05 MBq ml^{-1}					
CP	54.3 ± 2.3%	25.5 ± 1.3%	14.9 ± 0.7%	0.121 ± 0.1%	$<1.0^{*}10^{-36}$
SC-ST	50.7 ± 1.1%	36.8 ± 1.1%	13.2 ± 0.7%	1.65 ± 0.6%	0.440 ± 0.2%
SC-HS	69.9 ± 2.9%	72.6 ± 2.2%	28.8 ± 1.5%	11.4 ± 1.0%	5.08 ± 0.3%

3.6. Image uniformity comparison

Reconstructed images of the uniformity phantom filled with ^{18}F, along with the corresponding line profile analysis, are shown in figure 8.

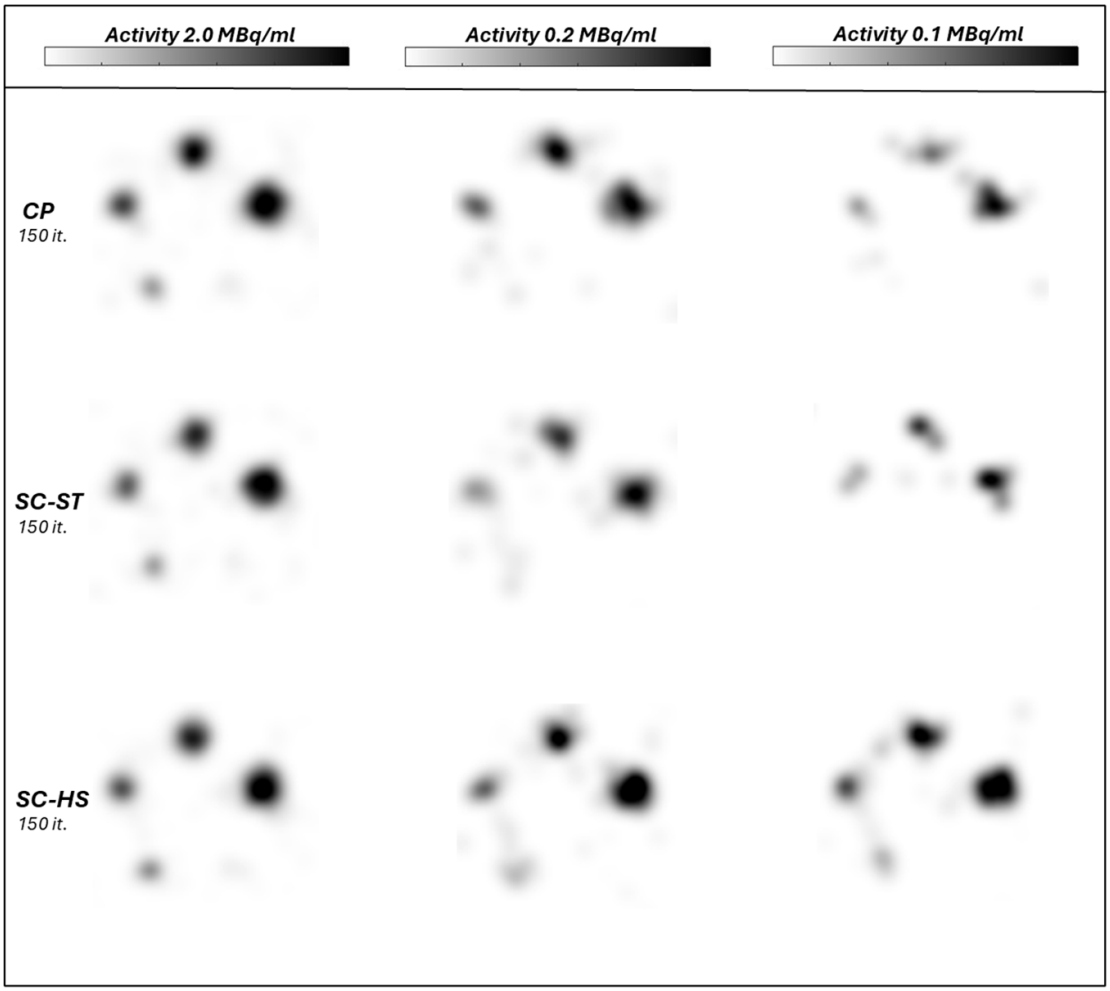

Figure 7. Images of the recovery phantom reconstructed using CP, SC-ST, and SC-HS collimators. Rods were uniformly filled with 2.0 MBq ml^{-1}, 0.2 MBq ml^{-1}, and 0.1 MBq ml^{-1} of ^{89}Zr. Images shown were post-filtered with a 3D Gaussian filter having a FWHM of 1.25 mm. The displayed images were generated by summing fifteen consecutive slices at the phantom's center, resulting in a final slice thickness of 6 mm.

Table 3. Recovery coefficients (RC), averaged over multiple runs, were calculated for all rods of the recovery phantom using both CP and SC collimators for ^{89}Zr. Errors represent the standard deviation across runs.

^{89}Zr–2.0 MBq ml^{-1}					
Collimator	RC rod 2.5 mm	RC rod 2.0 mm	RC rod 1.5 mm	RC rod 1.0 mm	RC rod 0.5 mm
CP	69.2 ± 3.5%	63.5 ± 2.3%	38.8 ± 1.8%	17.5 ± 0.9%	3.66 ± 0.5%
SC-ST	64.3 ± 3.5%	67.6 ± 3.0%	36.3 ± 1.3%	20.4 ± 0.7%	3.22 ± 0.4%
SC-HS	73.6 ± 0.8%	63.1 ± 1.6%	41.4 ± 1.8%	21.2 ± 0.7%	4.14 ± 0.5%
^{89}Zr–0.2 MBq ml^{-1}					
CP	61.3 ± 6.9%	49.0 ± 2.2%	28.7 ± 1.6%	3.42 ± 0.4%	$<1.0 * 10^{-6}$
SC-ST	54.5 ± 3.6%	50.5 ± 3.9%	22.4 ± 0.9%	5.36 ± 0.5%	$<1.0 * 10^{-34}$
SC-HS	69.4 ± 2.6%	54.9 ± 1.8%	32.0 ± 3.3%	12.5 ± 1.2%	$< 1.0 * 10^{-10}$
^{89}Zr–0.1 MBq ml^{-1}					
CP	37.4 ± 0.7%	22.1 ± 2.2%	13.3 ± 1.9%	$<1.0 * 10^{-10}$	$<1.0 * 10^{-19}$
SC-ST	46.5 ± 0.9%	28.7 ± 5.3%	10.8 ± 1.3%	$<1.0 * 10^{-4}$	$<1.0 * 10^{-30}$
SC-HS	63.7 ± 5.8%	46.6 ± 5.4%	26.3 ± 2.2%	8.46 ± 1.2%	$<1.0 * 10^{-15}$

Visual inspection of these images shows that all collimators produce comparable results, without distortions attributable to potential sampling issues.

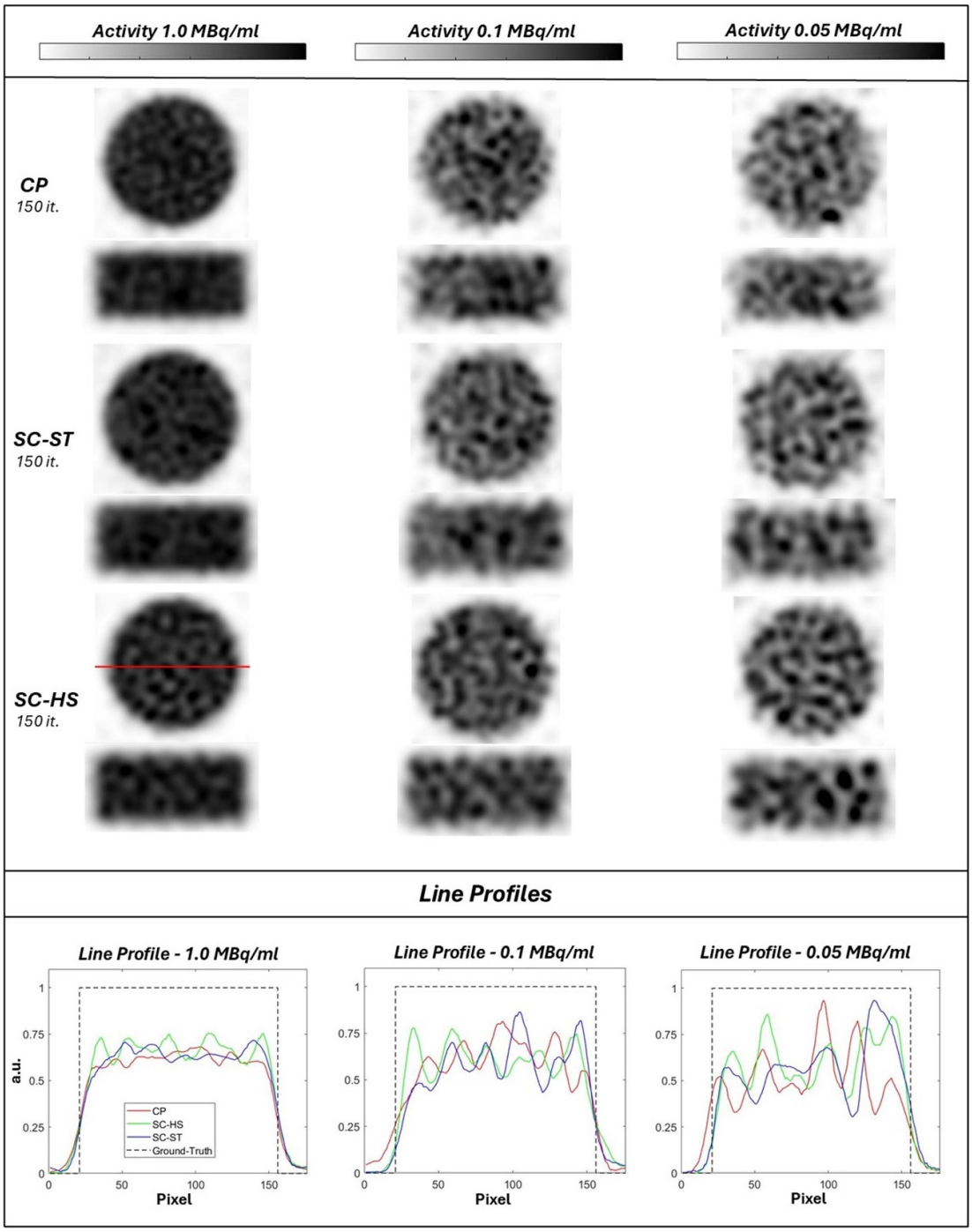

Figure 8. Images of the uniform phantom reconstructed using CP and SC collimators. The phantom was uniformly filled with 1.0 MBq ml^{-1}, 0.1 MBq ml^{-1}, and 0.05 MBq ml^{-1} of ^{18}F. A 3D Gaussian filter with a 1.25 mm FWHM was applied for post-filtering. The displayed images were generated by summing ten consecutive slices at the phantom's center, resulting in a final slice thickness of 4 mm. Line profiles were extracted for each configuration along the red line, which is shown only in one case for clarity.

Figure 9 presents the reconstructed images of the uniformity phantom filled with ^{89}Zr, together with the corresponding line profile analysis.

All collimators demonstrate comparable performance for ^{89}Zr, with no visible artifacts suggesting sampling issues.

Results for the quantitative analysis of image uniformity are reported in the appendix, tables A1 and A2.

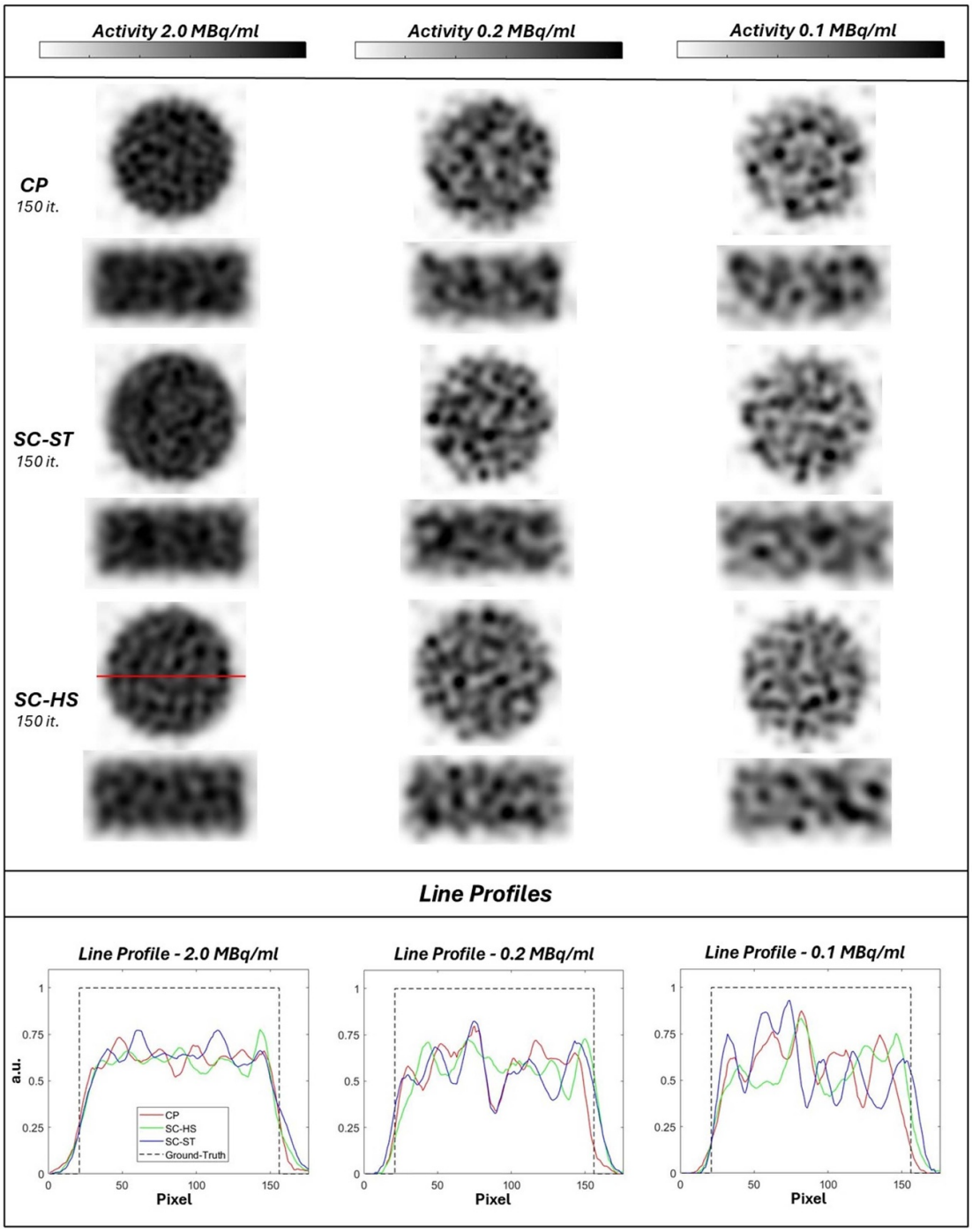

Figure 9. Images of the uniform phantom reconstructed using CP and SC collimators. The phantom was uniformly filled with 2.0 MBq ml^{-1}, 0.2 MBq ml^{-1}, and 0.1 MBq ml^{-1} of ^{89}Zr. A 3D Gaussian filter with a 1.25 mm FWHM was applied for post-filtering. The displayed images were generated by summing ten consecutive slices at the phantom's center, resulting in a final slice thickness of 4 mm. Line profiles were extracted for each configuration along the red line, which is shown only in one case for clarity.

4. Discussion

We presented results from a MC simulation study investigating a novel SC geometry designed to enhance sensitivity in multi-pinhole imaging across a wide energy range (25–1000 keV). This approach aims to support SPECT and PET studies conducted at low activity concentrations and/or with short scan durations. As part of our broader investigation of collimator optimization, we previously introduced the Twisted CP (TCP) design, showing that integrating narrower POAs into CP geometry could improve both spatial resolution and sensitivity (Cosmi *et al* 2024a). However, compared to the original CP the sensitivity gains were modest (15.6% for ^{18}F and 29.4% for ^{89}Zr), and the overall complexity remained

similar. Exploring a different approach, we here described the novel 'SC' design, featuring a simpler geometry with a more uniform distribution of pinholes across the collimator surface. This configuration provides greater flexibility in increasing pinhole diameter, reaching values not feasible with CP or TCP designs, while preserving the same CFOV. We performed comparative evaluations of sensitivity, image resolution, RCs, and uniformity between the SC and CP collimators using different activity concentrations of ^{18}F and ^{89}Zr. The results are summarized in figures 3–9 and tables 1–3.

The analysis of peak and CFOV-averaged sensitivity showed comparable sensitivities attained by the CP and SC-ST collimators (as expected by design), while the SC-HS design achieved improvements of approximately a factor of three for ^{18}F and a factor of two for ^{89}Zr compared to the CP collimator (table 1) as a result of the larger pinhole diameter.

In terms of image resolution, the CP and SC-ST collimators performed similarly for both ^{18}F and ^{89}Zr (figures 3 and 4), resolving the same rod sectors across all activity concentrations. These results indicate that the new geometry and sampling method of the SC design do not significantly affect the baseline performance of the collimator. Instead, image quality appears to be primarily governed by the resolution–sensitivity trade-off, which was identical for these two designs. By comparison, at the highest tested activity concentration, the SC-HS collimator showed slightly reduced performance with ^{18}F and comparable performance with ^{89}Zr. The reduced performance for ^{18}F is related to the expected resolution loss due to the larger pinhole diameter used in this configuration. The ^{89}Zr outcome presumably reflects a combination of two factors: lower intrinsic detector sensitivity and edge penetration effects both due to its high-energy prompt gammas. Because the SC-HS design combines the highest sensitivity with the smallest POAs among the tested designs, these effects were likely mitigated, resulting in performance comparable to that of the other collimators. At lower activity concentrations for both isotopes, the SC-HS outperformed the other collimators. These improvements can be attributed to a favorable adjustment of the resolution–sensitivity trade-off. At these activity levels, the increased sensitivity offset the resolution loss caused by the wider pinhole opening, ultimately resulting in more accurate and detailed reconstructions.

CNR analysis (figure 5) confirmed the visual assessment from figures 3 and 4, showing mostly comparable results within the margin of error for the CP and SC-ST collimators, and highlighting the improvements achieved by the SC-HS at lower activity concentrations.

The RCs extracted from the recovery phantom (figures 6 and 7) demonstrate a clear performance advantage of the SC-HS collimator, which outperformed both the SC-ST and CP designs (tables 2 and 3). This finding suggests that the increased sensitivity of the SC-HS enhances the system's ability to accurately localize the activity distribution. This improvement is likely due to the greater number of detected events, allowing the reconstruction algorithm to better differentiate between areas of true activity and regions dominated by background or noise. Such improvements are particularly relevant in quantitative studies conducted at low activity levels.

Finally, we investigated images of a uniform activity distribution with the purpose of analyzing the validity of the novel SC sampling strategy (figures 8 and 9). Visual inspection revealed no discernible differences among the three collimators, confirming that the new sampling strategy not introduce image artifacts. Significant data incompleteness would typically distort the shape of the uniform phantom, such as causing a convex appearance at its lateral edges, but these artifacts were not observed.

An important implication of the SC geometry is its flexibility, which permits the use of even larger pinhole diameters than those employed in the SC-HS configuration. Increasing the diameter further would enhance sensitivity and could therefore benefit studies conducted at lower activity concentrations than those presented in this work. However, such modifications may also increase multiplexing if the distance between pinholes is not increased. Higher multiplexing has been associated with reconstruction artifacts in highly multiplexed multi-pinhole systems (Mok *et al* 2011). In future work, the combination of larger pinholes with advanced de-multiplexing strategies, including approaches based on alternative pinholes with shutter devices as shown in (Beekman 2012) where de-multiplexing with pinholes was first presented, or more recently proposed alternative methods (Johnson *et al* 2014, Pells *et al* 2024), could be explored to balance these effects, allowing SC geometries to exploit higher sensitivity while mitigating the risk of image degradation. Another promising direction is the investigation of keel-edge pinholes within the SC framework. The current study focused on knife-edge pinholes to maintain consistency with the experimental imaging system. This choice was further supported by previous work comparing knife- and

keel-edge geometries (van der Have and Beekman 2006). Nevertheless, keel-edge designs could be particularly interesting for applications where penetration is the dominant concern.

It is worth highlighting that the simulated imaging system employs a 9.5 mm thick scintillator, which is not ideal for detecting high-energy prompt gammas such as the 511 keV or 909 keV emissions. Prior studies have shown that increasing the scintillator thickness to 19 mm or even 40 mm can approximately double or quadruple the detection efficiency for 511 keV gammas, improving it from around 12% to approximately 27% or 53%, respectively (Cosmi *et al* 2024b). A similar enhancement is expected for 909 keV gammas. Nonetheless, to focus on comparing collimator performance, we chose MILabs' standard detector configuration, which is more commonly used in practice and typically features 9.5 mm crystals, although 19 mm options are also available from this vendor.

More broadly, this work contributes to ongoing efforts to enhance image quality. We pursued this goal by introducing a new collimator design with improved sensitivity. It is worth noting, however, that various strategies targeting different system components can be implemented to improve image quality (Deprez *et al* 2014, Abbaspour *et al* 2017, Ma *et al* 2017, Massari *et al* 2019, Wei *et al* 2020). Furthermore, similar improvements can be achieved by focusing on optimizing image reconstruction techniques (Chun *et al* 2013, Dietze *et al* 2019, Ao *et al* 2021, Marquis *et al* 2021, Satyajit Ghosh *et al* 2025).

5. Conclusion

We described the SC collimator, a novel design featuring pinholes more evenly distributed across the collimator surface to enable both high-energy and high-sensitivity PET and SPECT imaging. Its performance was evaluated against that of a conventional CP collimator for which increasing the pinhole diameter is not possible due to geometric constraints. Results showed that the SC geometry introduced no imaging artifacts and enabled straightforward tuning of the resolution–sensitivity trade-off by increasing the pinhole diameter. This proved particularly advantageous at low activity concentrations of ^{18}F and ^{89}Zr, resulting in improved image quality and greater quantitative accuracy.

Data availability statement

All data that support the findings of this study are included within the article (and any supplementary information files).

Supplementary Line Profiles available at https://doi.org/10.1088/1361-6560/ae2e7a/data1.

Acknowledgment

This work was financed by the research grant QUARAT: Quantitative Universal Radiotracer Tomography (TTW16885) which is financed in part by the Dutch Research Council (NWO).

Conflict of interest

The authors declare no conflicts of interest to disclose.

Appendix

A.1. Simulation setup

Figure A1 shows the system geometry as modeled in GATE.

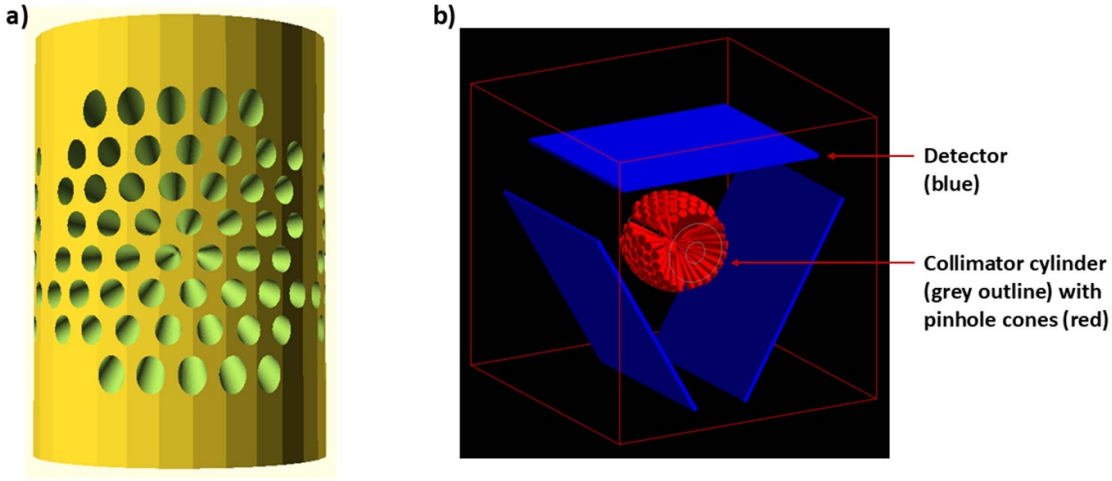

Figure A1. Visual representation of the collimator in 3D (a) and of the system geometry as modeled in GATE (b). The blue rectangles represent the three detectors arranged in a triangular setup. The grey outlines indicate the cylindrical collimator, while the red cones depict the pinhole cones. Light guides and PMTs were not explicitly simulated; instead, their effects were incorporated by assuming an intrinsic spatial resolution and energy resolutions consistent with the manufacturer's specifications.

A.2. Profile analysis

An analysis of the profiles through the smallest distinguishable sector was conducted. The results, presented in figure A2, support the observations from the visual inspection of figures 3 and 4 and are consistent with the CNR analysis shown in figure 5.

A.3. Quantitative uniformity analysis

Results of the quantitative analysis of the reconstructed uniformity images are reported in tables A1 and A2 for ^{18}F and ^{89}Zr, respectively.

Table A1. Results for average percentage uniformity obtained from multiple runs using CP and SC collimators for ^{18}F are presented. Reported values correspond to the final iteration (150) and include the standard deviations.

Collimator	Uniformity 1.0 MBq ml^{-1} (%)	Uniformity 0.1 MBq ml^{-1} (%)	Uniformity 0.05 MBq ml^{-1} (%)
CP	43.2 ± 2.8	61.9 ± 6.2	86.8 ± 5.5
SC-ST	46.2 ± 4.9	68.8 ± 5.5	79.6 ± 6.7
SC-HS	43.6 ± 1.9	60.3 ± 5.8	96.6 ± 4.4

For ^{18}F, the CP and SC-ST collimators demonstrated similar performance across all three activity concentrations, with differences remaining within the margin of error. In contrast, the SC-HS collimator showed comparable performance at 1.0 MBq ml^{-1} and 0.1 MBq ml^{-1}, but exhibited a slight decline of 10.7% at 0.05 MBq ml^{-1}.

Table A2. Results for average percentage uniformity obtained from multiple runs using CP and SC collimators for ^{89}Zr are presented. Reported values correspond to the final iteration (150) and include the standard deviations.

Collimator	Uniformity 2.0 MBq ml^{-1} (%)	Uniformity 0.2 MBq ml^{-1} (%)	Uniformity 0.1 MBq ml^{-1} (%)
CP	56.2 ± 6.0	87.5 ± 9.2	99.2 ± 3.8
SC-ST	41.2 ± 1.8	77.4 ± 11.2	98.1 ± 6.3
SC-HS	34.4 ± 0.9	70.1 ± 5.9	87.7 ± 4.6

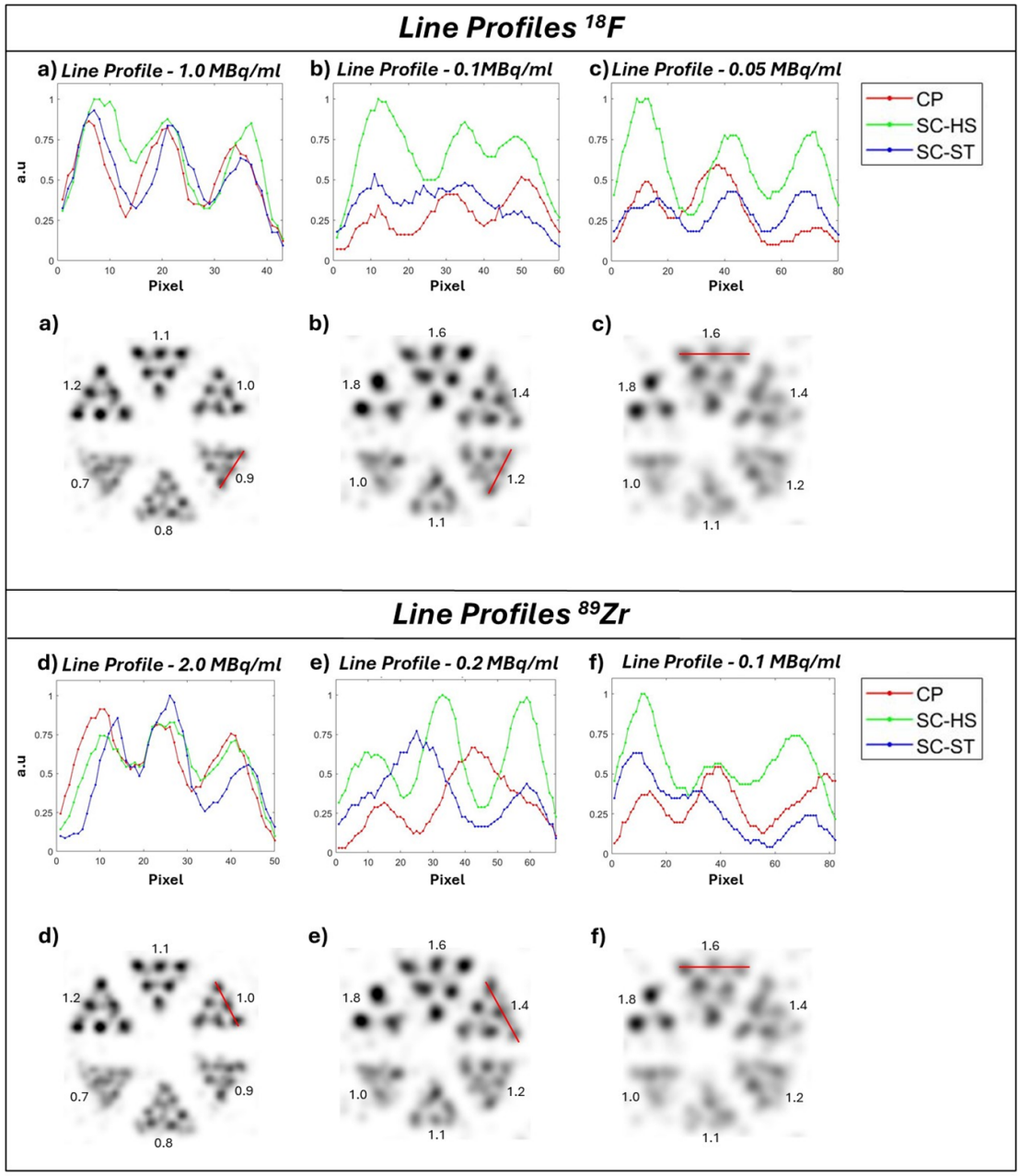

Figure A2. Profiles obtained from the resolution phantom images. The analysis was performed on the images in figures 3 and 4 using the results at 150 iterations. Panels (a)–(c) show the line profiles for ^{18}F, each corresponding to the rod sector marked by a red line in the resolution-phantom image with matching panel label (panels (a)–(c)). Panels (d)–(f) show the line profiles for ^{89}Zr, likewise matched to the rod sector indicated by a red line in the corresponding phantom image (panels (d)–(f)). The resolution phantom images reported in this figure were acquired using the SC-HS collimator.

For ^{89}Zr, at the highest activity concentration, both SC-ST and SC-HS outperformed CP, with SC-HS providing an improvement of 48.1% compared to CP. At 0.2 MBq ml^{-1}, SC-HS again achieved the best performance, showing a 22.1% improvement over CP. Finally, at 0.1 MBq ml^{-1}, CP and SC-ST delivered comparable results, while SC-HS offered a moderate improvement of 12.3%.

A.4. Uniformity at high activity concentration

Image uniformity at high activity concentrations (10 MBq ml^{-1} for ^{18}F and 20 MBq ml^{-1} for ^{89}Zr) was evaluated to assess whether design-dependent artifacts emerge under such conditions. The results, together with the corresponding line profile analysis, are presented in figure A3.

Visual inspection of this figure indicates that the novel collimator does not exhibit any noticeable design-dependent artifacts under high-statistics conditions.

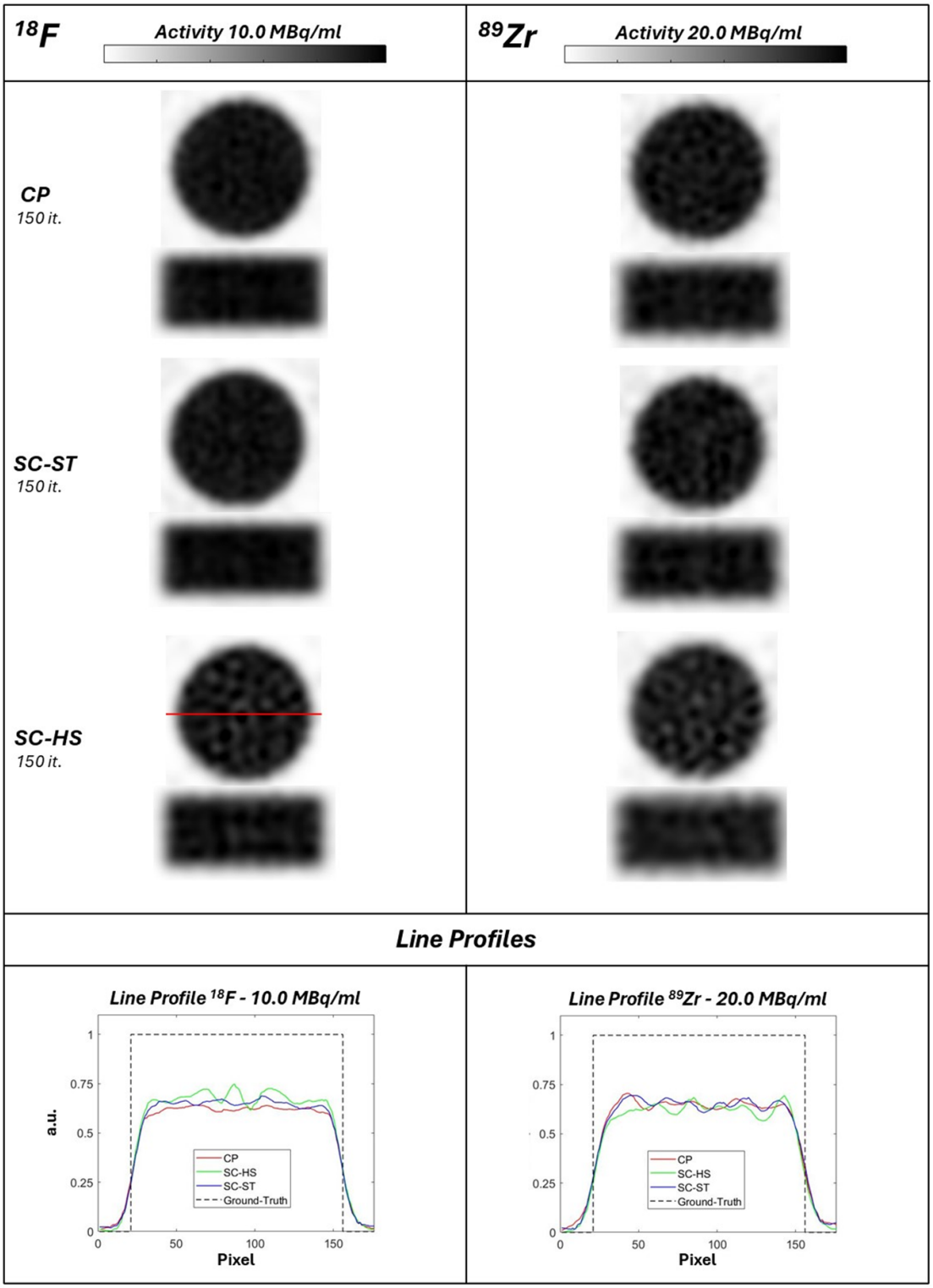

Figure A3. Images of the uniform phantom reconstructed using CP and SC collimators. The phantom was uniformly filled with 10.0 MBq ml^{-1} of ^{18}F or 20.0 MBq ml^{-1} of ^{89}Zr, respectively. A 3D Gaussian filter with a 1.25 mm FWHM was applied for post-filtering. The displayed images were generated by summing ten consecutive slices at the phantom's center, resulting in a final slice thickness of 4 mm. Line profiles were extracted for each configuration along the red line, which is shown only in one case for clarity.

ORCID iDs

Valerio Cosmi 0009-0008-2748-2202
Satyajit Ghosh 0000-0001-6334-1185
Marlies C Goorden 0009-0007-2202-5371

References

Abbaspour S, Mahmoudian B and Islamian J P 2017 Cadmium telluride semiconductor detector for improved spatial and energy resolution radioisotopic imaging *World J. Nucl. Med.* **16** 101–7

Alauddin M M 2012 Positron emission tomography (PET) imaging with (18)F-based radiotracers *Am. J. Nucl. Med. Mol. Imaging* **2** 55–76

Ao W Q, Li W B and Qian J L 2021 A data and knowledge driven approach for SPECT using convolutional neural networks and iterative algorithms *J. Inverse Ill-Posed Probl.* **29** 543–55

Beekman F J 2011 Focused pinhole gamma detection device *US Patent* 8,067,741 B2

Beekman F J 2012 A focused pinhole gamma detection device *MILabs B.V. Patent application NL* 2006107 EP2482101

Beekman F J 2022 *A SPECT scanner and collimator US Patent* 0133246 A1

Beekman F J, Kamphuis C, Koustoulidou S, Ramakers R M and Goorden M C 2021 Positron range-free and multi-isotope tomography of positron emitters *Phys. Med. Biol.* **66** 065011

Beekman F J and van der Have F 2007 The pinhole: gateway to ultra-high-resolution three-dimensional radionuclide imaging *Eur. J. Nucl. Med. Mol. Imaging* **34** 151–61

Bernsen M R, Vaissier P E B, Van Holen R, Booij J, Beekman F J and de Jong M 2014 The role of preclinical SPECT in oncological and neurological research in combination with either CT or MRI *Eur. J. Nucl. Med. Mol. Imaging* **41** S36–S49

Borjesson P K *et al* 2006 Performance of immuno-positron emission tomography with zirconium-89-labeled chimeric monoclonal antibody U36 in the detection of lymph node metastases in head and neck cancer patients *Clin. Cancer Res.* **12** 2133–40

Chun S Y, Fessler J A and Dewaraja Y K 2013 Correction for collimator-detector response in SPECT using point spread function template *IEEE Trans. Med. Imaging* **32** 295–305

Cosmi V, Kvassheim M, Ghosh S, Beekman F J and Goorden M C 2024a Twisted clustered pinhole collimation for improved high-energy preclinical SPECT/PET *Phys. Med. Biol.* **69** 225016

Cosmi V, Wang B, Goorden M C and Beekman F J 2024b NaI gamma camera performance for high energies: effects of crystal thickness, photomultiplier tube geometry and light guide thickness *Med. Phys.* **51** 4696–708

Crawford J R, Robertson A K H, Yang H, Rodríguez-Rodríguez C, Esquinas P L, Kunz P, Blinder S, Sossi V, Schaffer P and Ruth T J 2018 Evaluation of (209)At as a theranostic isotope for (209)At-radiopharmaceutical development using high-energy SPECT *Phys. Med. Biol.* **63** 045025

De Feo M S, Pontico M, Frantellizzi V, Corica F, De Cristofaro F and De Vincentis G 2022 Zr-PET imaging in humans: a systematic review *Clin. Transl. Imaging* **10** 23–36

de Swart J, Chan H S, Goorden M C, Morgenstern A, Bruchertseifer F, Beekman F J, de Jong M and Konijnenberg M W 2016 Utilizing high-energy gamma-photons for high-resolution 213Bi SPECT in mice *J. Nucl. Med.* **57** 486–92

Deprez K, Van Holen R and Vandenberghe S 2014 A high resolution SPECT detector based on thin continuous LYSO *Phys. Med. Biol.* **59** 153–71

Dietze M M A, Branderhorst W, Kunnen B, Viergever M A and de Jong H W A M 2019 Accelerated SPECT image reconstruction with FBP and an image enhancement convolutional neural network *EJNMMI Phys.* **6** 14

Esquinas P L, Rodríguez-Rodríguez C, Carlos De La Vega J, Bokharaei M, Saatchi K, Shirmohammad M, Häfeli U O, Sossi V and Celler A 2017 (188)Re image performance assessment using small animal multi-pinhole SPECT/PET/CT system *Phys. Med.* **33** 26–37

Franc B L *et al* 2008 Small-animal SPECT and SPECT/CT: important tools for preclinical investigation *J. Nucl. Med.* **49** 1651–63

GATE users guide (available at: https://opengate.readthedocs.io/en/latest/index.html)

Ghosh S *et al* 2025 Ultra-high energy spectral prompt PET *Phys. Med. Biol.* **70** 075010

Ghosh S, Cosmi V, Ramakers R M, Beekman F J and Goorden M C 2025 Dual-photopeak joint image reconstruction for pinhole SPECT, PET and PET-SPECT *Phys. Med. Biol.* accepted (https://doi.org/10.1088/1361-6560/ae2ce0)

Goorden M C and Beekman F J 2010 High-resolution tomography of positron emitters with clustered pinhole SPECT *Phys. Med. Biol.* **55** 1265–77

Goorden M C, Kamphuis C, Ramakers R M and Beekman F J 2020 Accelerated image reconstruction by a combined dual-matrix dual-voxel approach *Phys. Med. Biol.* **65** 105014

Goorden M C, van der Have F, Kreuger R, Ramakers R M, Vastenhouw B, Burbach J P H, Booij J, Molthoff C F M and Beekman F J 2013 VECTor: a preclinical imaging system for simultaneous submillimeter SPECT and PET *J. Nucl. Med.* **54** 306–12

Goorden M C, van Roosmalen J, van der Have F and Beekman F J 2016 Optimizing modelling in iterative image reconstruction for preclinical pinhole PET *Phys. Med. Biol.* **61** 3712–33

Ivashchenko O *et al* 2015 Ultra-high-sensitivity submillimeter mouse SPECT *J. Nucl. Med.* **56** 470–5

Ivashchenko O, van der Have F, Villena J L, Groen H C, Ramakers R M, Weinans H H and Beekman F J 2014 Quarter-millimeter-resolution molecular mouse imaging with U-SPECT(+) *Mol. Imaging* **13** 7290–2014

Johnson L C, Shokouhi S and Peterson T E 2014 Reducing multiplexing artifacts in multi-pinhole SPECT with a stacked silicon-germanium system: a simulation study *IEEE Trans. Med. Imaging* **33** 2342–51

Koniar H, Wharton L, Ingham A, Rodríguez-Rodríguez C, Kunz P, Radchenko V, Yang H, Rahmim A, Uribe C and Schaffer P 2024 quantitative SPECT imaging of actinium-226: feasibility and proof-of-concept *Phys. Med. Biol.* **69** 155003

Ma T Y, Haedicke K and Grimm J 2017 Development of a SiPM based preclinical PET SPECT imaging system imaging system *J. Nucl. Med.* **59** 58

Marquis H, Deidda D, Gillman A, Willowson K P, Gholami Y, Hioki T, Eslick E, Thielemans K and Bailey D L 2021 Theranostic SPECT reconstruction for improved resolution: application to radionuclide therapy dosimetry *EJNMMI Phys.* **8** 16

Massari R, D'Elia A and Soluri A 2019 A new high-resolution imaging system (HiRIS2) detector for preclinical SPECT imaging *Nucl. Instrum. Methods Phys. Res. A* **917** 25–30

MILabs 2024 *VECTor Collimators Datasheet* (MILabs B.V)

Mok G S P, Wang Y C and Tsui B M W 2009 Quantification of the multiplexing effects in multi-pinhole small animal SPECT: a simulation study *IEEE Trans. Nucl. Sci.* **56** 2636–43

Mok G S, Tsui B M and Beekman F J 2011 The effects of object activity distribution on multiplexing multi-pinhole SPECT *Phys. Med. Biol.* **56** 2635–50

National Electrical Manufacturers Association (NEMA) 2008 NEMA standards publication NU 4-2008: performance measurements of small animal positron emission tomographs

Nguyen M P *et al* 2022 Ultra-high sensitivity simultaneous small animal PET-SPECT for microCi range imaging *J. Nucl. Med.* **63** 2344

Ogawa K, Echigo H, Mishiro K, Hirata S, Washiyama K, Kitamura Y, Takahashi K, Shiba K and Kinuya S 2021 Ga- and at-labeled RGD peptides for radiotheranostics with multiradionuclides *Mol. Pharmaceut.* **18** 3553–62
Ogawa K, Harata Y, Ichihara T, Kubo A and Hashimoto S 1991 A practical method for position-dependent Compton-scatter correction in single photon emission CT *IEEE Trans. Med. Imaging* **10** 408–12
Pells S, Zeraatkar N, Kalluri K S, Moore S C, May M, Furenlid L R, Kupinski M A, Kuo P H and King M A 2024 Correction of multiplexing artefacts in multi-pinhole SPECT through temporal shuttering, de-multiplexing of projections, and alternating reconstruction *Phys. Med. Biol.* **69** 125004
Reivich M *et al* 1979 The [18F]fluorodeoxyglucose method for the measurement of local cerebral glucose utilization in man *Circ. Res.* **44** 127–37
Robertson A K H, Ramogida C F, Rodríguez-Rodríguez C, Blinder S, Kunz P, Sossi V and Schaffer P 2017 Multi-isotope SPECT imaging of the (225)Ac decay chain: feasibility studies *Phys. Med. Biol.* **62** 4406–20
Rowland D J and Cherry S R 2008 Small-animal preclinical nuclear medicine instrumentation and methodology *Semin. Nucl. Med.* **38** 209–22
Saeedi Saghez B, Rodríguez-Rodríguez C, Esquinas P L, Merkens H, Bénard F, Radchenko V and Yang H 2024 First preclinical SPECT/CT imaging and biodistribution of [(165)Er]ErCl(3) and [(165)Er]Er-PSMA-617 *EJNMMI Radiopharm. Chem.* **9** 90
Sigurdsson B *et al* 2023 A SPECT-based method for dynamic imaging of the glymphatic system in rats *J. Cereb. Blood Flow Metab.* **43** 1153–65
Vaissier P E, Beekman F J and Goorden M C 2016 Similarity-regulation of OS-EM for accelerated SPECT reconstruction *Phys. Med. Biol.* **61** 4300–15
Vaissier P E, Goorden M C, Vastenhouw B, van der Have F, Ramakers R M and Beekman F J 2012 Fast spiral SPECT with stationary gamma-cameras and focusing pinholes *J. Nucl. Med.* **53** 1292–9
Vallabhajosula S 2007 F-Labeled positron emission tomographic radiopharmaceuticals in oncology:: an overview of radiochemistry and mechanisms of tumor localization *Semin. Nucl. Med.* **37** 400–19
van der Have F and Beekman F J 2006 Penetration, scatter and sensitivity in channel micro-pinholes for SPECT: a Monte Carlo investigation *IEEE Trans. Nucl. Sci.* **53** 2635–45
van der Have F, Ivashchenko O, Goorden M C, Ramakers R M and Beekman F J 2016 High-resolution clustered pinhole (131)Iodine SPECT imaging in mice *Nucl. Med. Biol.* **43** 506–11
van der Have F, Vastenhouw B, Ramakers R M, Branderhorst W, Krah J O, Ji C, Staelens S G and Beekman F J 2009 U-SPECT-II: an ultra-high-resolution device for molecular small-animal imaging *J. Nucl. Med.* **50** 599–605
Vastenhouw B and Beekman F J 2007 Submillimeter total-body murine imaging with U-SPECT-I *J. Nucl. Med.* **48** 487–93
Visser E P *et al* 2011 Image quality phantom and parameters for high spatial resolution small-animal SPECT *Eur. J. Nucl. Med. Mol. Imaging* **38** S173
Vosjan M J, Perk L R, Visser G W M, Budde M, Jurek P, Kiefer G E and van Dongen G A M S 2010 Conjugation and radiolabeling of monoclonal antibodies with zirconium-89 for PET imaging using the bifunctional chelate p-isothiocyanatobenzyl-desferrioxamine *Nat. Protoc.* **5** 739–43
Walker M D, Goorden M C, Dinelle K, Ramakers R M, Blinder S, Shirmohammad M, van der Have F, Beekman F J and Sossi V 2014 Performance assessment of a preclinical PET scanner with pinhole collimation by comparison to a coincidence-based small-animal PET scanner *J. Nucl. Med.* **55** 1368–74
Wei Q Y, Ma T, Jiang N, Xu T, Lyu Z, Hu Y and Liu Y 2020 A side-by-side LYSO/GAGG phoswich detector aiming for SPECT imaging *Nucl. Instrum. Methods Phys. Res. A* **953** 163242
Wharton L *et al* 2024 Preclinical evaluation of MC1R targeting theranostic pair [(155)Tb]Tb-crown-alphaMSH and [(161)Tb]Tb-crown-alphaMSH *Nucl. Med. Biol.* **136-137** 108925
Wouters A, Simon K M and Hirschberg J G 1973 Direct method of decoding multiple images *Appl. Opt.* **12** 1871–3
Wu C, de Jong J R, Gratama van Andel H A, van der Have F, Vastenhouw B, Laverman P, Boerman O C, Dierckx R A J O and Beekman F J 2011 Quantitative multi-pinhole small-animal SPECT: uniform versus non-uniform Chang attenuation correction *Phys. Med. Biol.* **56** N183–93
Wu C, van der Have F, Vastenhouw B, Dierckx R A J O, Paans A M J and Beekman F J 2010 Absolute quantitative total-body small-animal SPECT with focusing pinholes *Eur. J. Nucl. Med. Mol. Imaging* **37** 2127–35